

A Faraday Rotation Study of the Stellar Bubble and H II Region Associated with the W4 Complex

Allison H. Costa¹ and Steven R. Spangler¹

ABSTRACT

We utilized the Very Large Array to make multifrequency polarization measurements of 20 radio sources viewed through the IC 1805 HII region and “Superbubble”. The measurements at frequencies between 4.33 and 7.76 GHz yield Faraday rotation measures (RMs) along 27 lines of sight to these sources. The RMs are used to probe the plasma structure of the IC 1805 HII region and to test the degree to which the Galactic magnetic field is heavily modified (amplified) by the dynamics of the HII region. We find that IC 1805 constitutes a “Faraday rotation anomaly”, or a region of increased RM relative to the general Galactic background value. The $|\text{RM}|$ due to the nebula is commonly $600 - 800 \text{ rad m}^{-2}$. However, the observed RMs are not as large as predicted by simplified analytic models that include substantial amplification of the Galactic magnetic field within the shell. The magnitudes of the observed RMs are consistent with shells in which the Galactic field is unmodified, or increased by a modest factor, such as due to magnetic flux conservation. We also find that with one exception, the sign of the RM is that expected for the polarity of the Galactic field in this direction. Finally, our results show intriguing indications that some of the largest values of $|\text{RM}|$ occur for lines of sight that pass outside the fully ionized shell of the IC 1805 HII region but pass through the Photodissociation Region associated with IC 1805.

Subject headings: ISM: bubbles, ISM: H II regions, ISM: magnetic fields, plasmas

1. Introduction

Young massive stars in OB associations photoionize the surrounding gas, creating an H II region, and their powerful stellar winds can inflate a bubble around the star cluster. Magnetic fields are important to the dynamics of these structures (Tomisaka 1990; Ferrière et al. 1991; Vallée 1993; Tomisaka 1998; Haverkorn et al. 2004; Sun et al. 2008; Stil et al. 2009), and they can elongate the cavity preferentially in the direction of the magnetic field and thicken the shell perpendicular to the field (Ferrière et al. 1991; de Avillez & Breitschwerdt 2005; Stil et al. 2009), causing deviations from the classical structure of the Weaver et al. (1977) wind-blown bubble. Knowledge of the magnitude and direction of the magnetic field within stellar bubbles and H II regions is important

¹Department of Physics and Astronomy, University of Iowa, Iowa City, Iowa 52242

for simulations and for understanding how the magnetic field interacts with and modifies these structures.

In previous work (i.e., Savage et al. 2013 and Costa et al. 2016), we investigated whether the Galactic magnetic field is amplified in the shell of the Rosette Nebula, an H II region and stellar bubble associated with NGC 2244 ($\ell = 206.5^\circ$, $b = -2.1^\circ$). Other similar work investigating magnetic fields near massive star clusters has been done by Harvey-Smith et al. (2011) and Purcell et al. (2015). In this work, we continue our investigation of how H II regions and stellar bubbles modify the ambient Galactic magnetic field by considering another example of a young star cluster and an H II region that appears to be formed into a shell by the effect of stellar winds.

1.1. Faraday Rotation and Magnetic Fields in the Interstellar Medium

Faraday rotation measurements probe the line of sight (LOS) component of the magnetic field in ionized parts of the interstellar medium (ISM), provided there is an independent estimate of the electron density. Faraday rotation is the rotation in the plane of polarization of a wave as it passes through magnetized plasma and is described by the equation

$$\chi = \chi_0 + \left[\left(\frac{e^3}{2\pi m_e^2 c^4} \right) \int n_e \mathbf{B} \cdot d\mathbf{s} \right] \lambda^2, \quad (1)$$

where χ is the polarization position angle, χ_0 is the intrinsic polarization position angle, the quantities in the parentheses are the usual standard physical constants in cgs units, n_e is the electron density, \mathbf{B} is the vector magnetic field, $d\mathbf{s}$ is the incremental path length interval along the LOS, and λ is the wavelength. We define the terms in the square bracket as the rotation measure, RM, and we can express the RM in mixed but convenient interstellar units as

$$\text{RM} = 0.81 \int n_e \text{ (cm}^{-3}\text{)} \mathbf{B} \text{ (}\mu\text{G)} \cdot d\mathbf{s} \text{ (pc)} \text{ rad m}^{-2}. \quad (2)$$

1.2. The H II Region and Stellar Bubble Associated with the W4 Complex

The H II region and stellar bubble of interest for the present study is IC 1805, which is located in the Perseus Arm. The star cluster responsible for the H II region and stellar bubble is OCl 352, which is a young cluster (1–3 Myr) (Basu et al. 1999). OCl 352 has 60 OB stars (Shi & Hu 1999). Three of these are the O stars HD 15570, HD 15558, and HD 15629, and they have mass loss rates between 10^{-6} and $10^{-5} M_\odot \text{ yr}^{-1}$ (Massey et al. 1995) and terminal wind velocities of 2200 – 3000 km s^{-1} (Garmany 1988; Groenewegen et al. 1989; Bouret et al. 2012). We adopt the nominal center of the star cluster to be R.A.(J2000) = $02^h 23^m 42^s$, decl.(J2000) = $+61^\circ 27' 0''$ ($\ell = 134.73$, $b = +0.92$) (Guetter & Vrba 1989) and a distance of 2.2 kpc to IC 1805 to conform with previous studies of the region (e.g., Normandeau et al. 1996; Dennison et al. 1997; Reynolds et al. 2001;

Terebey et al. 2003; Gao et al. 2015). In the literature, other distance values include: 2.35 kpc (Massey et al. 1995; Basu et al. 1999; West et al. 2007; Lagrois et al. 2012), 2 kpc (Dickel 1980), 2.04 kpc (Feigelson et al. 2013; Townsley et al. 2014), and 2.4 ± 0.1 kpc (Guetter & Vrba 1989).

We refer to the H II region between $-0.2^\circ < b < 2^\circ$ as IC 1805. This structure is also known as the Heart Nebula for its appearance at optical wavelengths. We differentiate this region from the northern latitudes that constitute the W4 Superbubble (Normandeau et al. 1996; West et al. 2007; Gao et al. 2015), and we use the nomenclature of W4 to describe the entire region, which includes IC 1805 and the W4 Superbubble. Below we summarize the structure of IC 1805 and Figure 1 is a cartoon diagram of the structure described here.

- *South.* On the southern portion of IC 1805, there is a loop structure of ionized material at $134^\circ < \ell < 136^\circ$, $b < 1^\circ$, which we call the southern loop. Terebey et al. (2003) find that at far infrared and radio wavelengths, the shell structure is well defined and ionization bounded, since the ionized gas lies interior to the dust shell. However, they also find that there is warm dust that extends past the southern loop and a faint ionized halo (see their Figure 6). Terebey et al. (2003) argue that the shell is patchy and inhomogeneous in density, which allows ionizing photons to escape. Gray et al. (1999) discuss extended emission surrounding IC 1805 and suggest that it may be evidence of an extended H II region (Anantharamaiah 1985). Also surrounding IC 1805 are patchy regions of H I (Braunsfurth 1983; Hasegawa et al. 1983; Sato 1990) and CO (Heyer & Terebey 1998; Lagrois & Joncas 2009a).

Terebey et al. (2003) model the structure of the southern loop using radio continuum data. They assume a spherical shell and place OCl 352 at the top edge of the bubble instead of at the center to accommodate spherical symmetry (see their Figures 4 and 5). The center of their shell model is at $(\ell, b) = (135.02^\circ, 0.42^\circ)$. They find an inner radius of 30 arcmin (19 pc) and a shell thickness of 10 arcmin (6 pc) and 2.5 arcmin (2 pc) for a thick and thin shell model, respectively. Terebey et al. (2003) report electron densities of 10 cm^{-3} and 20 cm^{-3} for the thick and thin shell models, respectively (see Section 3.5 and Table 3 of Terebey et al. 2003). While we utilize and discuss these models in the following sections, the center position of the shell in Terebey et al. (2003) was selected to fit the ionized shell, and as such, the shell parameters should only be used to describe the bottom of IC 1805. For latitudes near the star cluster, the model fails, as the star cluster is at the top edge of the bubble instead of at the center.

- *East.* On the eastern edge of IC 1805 ($\ell > 134.6^\circ$, $b < 0.9^\circ$), Terebey et al. (2003) find that warm dust extends outside the loop boundary and suggest that if the warm dust is associated with the ionized gas, then the bubble has blown out on the eastern side of IC 1805. At the Galactic latitude equal to the star cluster, the ionized gas appears to be pinched (Basu et al. 1999), which is usually caused by higher densities. There is a clump of CO emission in the vicinity of the eastern pinch at $(\ell, b) = (135.2^\circ, 1.0^\circ)$ (Lagrois & Joncas 2009a), and there is H I emission on the eastern edge at $(\ell, b) \geq (136^\circ, 0.5^\circ)$ (see Figure 1 of Sato 1990).

- *West.* On the western edge of IC 1805 is the W3 molecular cloud and the W3 complex, which hosts a number of compact H II regions and young stellar objects (see Bik et al. 2012 and their Figure 1). Dickel (1980) modeled the structure of W3, which is thought to be slightly in front of W4, and they argue that the advancement of the IC 1805 ionization front and shock front into the W3 molecular cloud may have triggered star formation. Moore et al. (2007) similarly conclude that the W3 molecular cloud has been compressed on one side by the expansion of IC 1805. While infrared sources nestled between the western edge of IC 1805 and eastern edge of the W3 molecular cloud are thought to be the product of this interaction, W3 Main, W3 (OH), and W3 North are thought to be sites of triggered star formation from IC 1795, which is part of W3 as well and not from the expansions of the ionization front (Nakano et al. 2017; Jose et al. 2016; Kiminki et al. 2015). There is therefore uncertainty regarding a physical connection between W3 and IC 1805.
- *North.* North of OCl 352, the bubble opens up into what is called the W4 Superbubble (Normandeau et al. 1997; Dennison et al. 1997; West et al. 2007; Gao et al. 2015), which is a sealed “egg-shaped” structure that extends up to $b \sim 7^\circ$ (Dennison et al. 1997; West et al. 2007). At the latitude of the star cluster, Lagrois & Joncas (2009a) estimate the distance between the eastern and western shell to be $\sim 1.2^\circ$ (46 pc) that increases in size up to 1.6° (61 pc) at $b = 1.8^\circ$ (see Figure 11 of Lagrois & Joncas 2009a). At higher latitudes, Dennison et al. (1997) model the thickness of the shell to be between 10–20 pc (16 – 31 arcminutes) from H α observations.

The “v”-shaped feature seen in Figure 2 at $(\ell, b) \sim (134.8^\circ, 1.35^\circ)$ is prominent in the ionized emission, and Heyer et al. (1996) report a cometary-shaped molecular cloud near $(\ell, b) \sim (134.8^\circ, 1.35^\circ)$. The alignment of the cometary cloud, as it is pointed towards IC 1805, suggests that the UV photons from the star cluster are responsible for the “v” shaped feature in the ionized emission on the side closest to the star cluster (Dennison et al. 1997; Taylor et al. 1999). Lagrois & Joncas (2009a) argue, from radial velocity measurements, that the cloud is located on the far side of the bubble wall, and while it may appear to be a cap to the bubble connecting to the southern loop, it is simply a projection effect. As such, the ridge of ionized material directly north of OCl 352 is not the outer radius of the shell but is part of the rear bubble wall.

- *PDR.* The H I and molecular emission near the southern ($\ell < 0.9^\circ$) portions of IC 1805 suggest that a Photodissociation Region (PDR) has formed exterior to the H II region. PDRs are the transition layer between the fully ionized H II region and molecular material, where far UV photons can propagate out and photodissociate molecules. We discuss the importance and observational evidence of a PDR in Section 5.3.

There is an extensive literature on the W4 region and its relationship to W3, dealing with the morphology (Dickel 1980; Dickel et al. 1980; Braunsfurth 1983; Normandeau et al. 1996; Dennison et al. 1997; Heyer & Terebey 1998; Taylor et al. 1999; Basu et al. 1999; Terebey et al. 2003; Lagrois

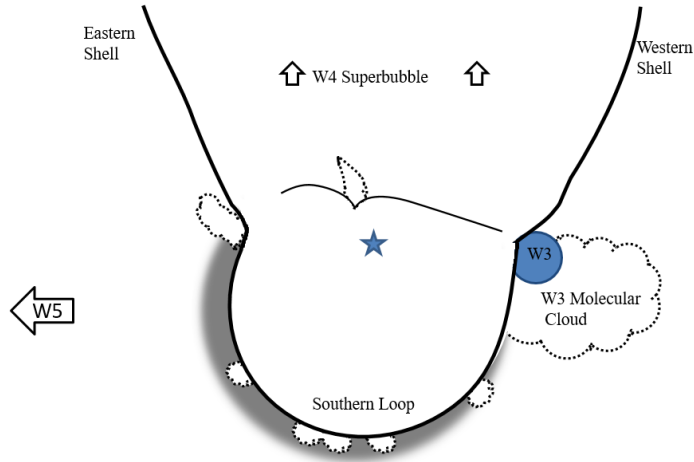


Fig. 1.— Cartoon of structure of IC 1805 and the surrounding region, which includes the W3 molecular cloud, W3 (blue filled circle), and the W4 Superbubble. The solid black lines represent the bright ionized shell in Figure 2, the dotted lines show molecular material from Lagrois & Joncas (2009a), and the gray shading represents the extended halo or PDR. The star represents the center of the exciting star cluster, OCl 352.

& Joncas 2009a,b; Stil et al. 2009) and star formation history (Carpenter et al. 2000; Oey et al. 2005). In the following paragraphs, we summarize those results from the literature that are most relevant to our polarimetric study and inferences on magnetic fields in this region.

Measurements of the total intensity and polarization of the Galactic nonthermal emission in the vicinity of H II regions are of interest because the H II regions and environs act as a Faraday-rotating screen inserted between the Galactic emission behind the H II region and that in front. Few radio polarimetric studies exist in the literature to date of the IC 1805 stellar bubble. Gray et al. (1999) present their polarimetric results of the W3/W4 region at 1420 MHz with the Dominion Radio Astrophysical Observatory (DRAO) Synthesis Telescope. They find zones of strong depolarization near the H II regions, particularly in the south, where there is a halo of extended emission around IC 1805. They conclude that RM values on order 10^3 rad m^{-2} and spatial RM gradients must exist to explain the depolarization near the H II region. More recently, Hill et al. (2017) present results of their polarimetric study of the Fan region ($\ell \sim 130^\circ$, $-5^\circ \leq b \leq +10^\circ$), which is a large structure in the Perseus arm that includes W3/W4. While the focus of their study was not on W4 specifically, they find similar results to Gray et al. (1999) in that there is sufficient Faraday rotation to cause beam depolarization in the regions of extended emission.

In the W4 Superbubble, West et al. (2007) determined the LOS magnetic field strength by estimating depolarization effects along adjacent lines of sight. Using estimates of the shell thickness and the electron density from Dennison et al. (1997), West et al. (2007) estimate $B_{\text{LOS}} \sim 3.4 - 9.1$

μG for lines of sight at $b > 5^\circ$. Gao et al. (2015) also report B_{LOS} estimates in the W4 Superbubble by assuming a passive Faraday screen model (Sun et al. 2007) and measuring the polarization angle for lines of sight interior and exterior to the screen. For the western shell ($\ell \sim 132.5^\circ$, $4^\circ < b < 6^\circ$) and the eastern shell ($\ell \sim 136^\circ$, $6^\circ < b < 7.5^\circ$) in the superbubble, Gao et al. (2015) report negative RMs between -70 and -300 rad m^{-2} in the western shell and positive RMs on order $+55 \text{ rad m}^{-2}$ in the eastern shell. Gao et al. (2015) conclude that the sign reversal is expected in the case of the Galactic magnetic field being lifted out of the plane by the expanding bubble. With $\text{H}\alpha$ estimates from Dennison et al. (1997) for the electron density and geometric arguments for the shell radii of the W4 Superbubble, Gao et al. (2015) estimate $|B_{\text{LOS}}| \sim 5 \mu\text{G}$.

Stil et al. (2009) compare their magnetohydrodynamic simulations of superbubbles to the W4 Superbubble. In general, they find that the largest Faraday rotation occurs in a thin region around the cavity, and inside the cavity, it would be smaller. They also present two limiting cases for the orientation of the Galactic magnetic field with respect to the line of sight, and the consequences for the RMs through the shell. If the Galactic magnetic field is perpendicular to the observer’s line of sight, then the contributions to the RM from the front and rear bubble wall would be of equal but opposite magnitude, except for small asymmetries which would lead to low RMs ($\sim 20 \text{ rad m}^{-2}$) through the cavity. This requires the magnetic field to be bent by the bubble to have a non-zero line of sight component. If the Galactic magnetic field is parallel to the line of sight, then the RMs through the front and rear bubble wall reinforce each other, and there are high RMs for lines of sight through the shell. In this case, there are higher RMs ($\sim 3 \times 10^3 \text{ rad m}^{-2}$) everywhere.

There are also studies of the magnetic field for W3. From H I Zeeman observations, van der Werf & Goss (1990) conclude that the B_{LOS} has small-scale structures that can vary on order of $50 \mu\text{G}$ over ~ 9 arcsec scales. Roberts et al. (1993) report values of the LOS magnetic field from H I Zeeman observations towards three resolved components of W3. The three components are near $(\ell, b) \sim (133.7^\circ, 1.21^\circ)$, with a maximum separation of 1.5 arcmin, and the LOS magnetic field is between $-50 \mu\text{G}$ and $+100 \mu\text{G}$. Balser et al. (2016) observed carbon radio recombination line (RRL) widths to estimate the total magnetic field strength in the photodissociation region (see Roshi 2007 for details). They report $B_{\text{tot}} = 140 - 320 \mu\text{G}$ near W3A ($133.72^\circ, 1.22^\circ$) and argue that for a random magnetic field, $B_{\text{tot}} = 2 |B_{\text{LOS}}|$, which would then be consistent with the Roberts et al. (1993) estimates of the B_{LOS} . It should be noted that these magnetic field strengths are substantially larger than those inferred for the W4 Superbubble on the basis of polarimetry of the Galactic background (see text above).

In this paper, we present new Faraday rotation results for IC 1805 to investigate the role of the magnetic field in the H II region and stellar bubble. As in Savage et al. (2013) and Costa et al. (2016), we utilize an arguably simpler and more direct method of inferring the LOS component of the magnetic field in H II regions. This is the measurement of the Faraday rotation of nonthermal background sources (usually extragalactic radio sources) whose lines of sight pass through the H II region and its vicinity. In Section 2, we describe the instrumental configuration and observations, including source selection. Section 3 details the data reduction process, including the methods used

to determine RM values. In Section 4, we report the results of the RM analysis and discuss Faraday rotation through the W4 complex in Section 5. We present models for the RM within the H II region and stellar bubble in Section 6. We discuss our observational results and their significance for the nature of IC 1805 in Section 7 and compare the results of this study with our previous study of the Rosette nebula in Section 8. We discuss future research in Section 9, and present our conclusions and summary in Section 10.

2. Observations

2.1. Source Selection

Our criteria for source selection were identical to Savage et al. (2013) and Costa et al. (2016) in that we searched the National Radio Astronomy Observatory Very Large Array Sky Survey (NVSS, Condon et al. 1998) database for point sources within 1° of OCl 352 (the “I” sources) with a minimum flux density of 20 mJy. We also searched in an annulus centered on the star cluster with inner and outer radii of 1° and 2° for outer sources (“O”) to measure the background RM due to the general ISM. We identified 31 inner sources and 26 outer sources in the region. We then inspected the NVSS postage stamps to ensure that they were point sources at the resolution of the NVSS (~ 45 arcseconds). We discarded sources that showed extended structure similar to Galactic sources. We selected 24 inner sources and 8 outer sources from this final list.

The sources are listed in Table 1, where the first column lists the source name in our nomenclature. The second and third columns list the right ascension (α) and declination (δ) of the observed sources. The positions are determined with the IMFIT task in CASA, which fits a 2D Gaussian to the intensity distribution at 4.33 GHz. Columns four and five give the Galactic longitude (ℓ), Galactic latitude (b), which is converted from α and δ using the Python *Astropy* package, and the angular separation from the center of the nebula (ξ) is given in column six. Column seven lists the flux density at 4.33 GHz calculated with IMFIT, and column eight gives the mean percent linear polarization ($m = P/I$) as measured across the eight 128 MHz maps and assuming a *Faraday simple* source. Figure 2 is a radio continuum mosaic from the Canadian Galactic Plane Survey (CGPS) (Taylor et al. 2003; Landecker et al. 2010) with the location of the sources, along with the names, indicated with filled circles.

Table 1: List of Sources Observed

Source Name	α (J2000) h m s	δ (J2000) ° ' "	\underline{l} (°)	\underline{b} (°)	ξ^a (arcmin)	$S_{4.33\text{GHz}}$ (mJy)	m (%)
W4-I1	02 30 16.2	+62 09 37.9	134.19	1.47	46.0	77	4
W4-I2	02 38 34.2	+61 08 46.6	135.49	0.91	46.2	5	12
W4-I3	02 36 45.5	+60 55 48.8	135.38	0.63	42.8	82	3
W4-I4	02 27 59.8	+62 15 44.0	133.91	1.47	58.9	46	10
W4-I5 ^b	02 28 01.6	+62 02 16.7	133.99	1.26	48.4	—	—
W4-I6	02 38 19.9	+61 08 03.5	135.47	0.89	44.8	12	11
W4-I7 ^b	02 27 33.8	+61 55 58.1	133.98	1.14	46.6	—	—
W4-I8	02 38 10.1	+62 08 57.0	135.05	1.81	57.1	47	9
W4-I9	02 28 21.6	+61 28 36.5	134.23	0.75	31.1	—	—
W4-I10 ^b	02 29 13.0	+61 00 53.4	134.50	0.36	36.2	—	—
W4-I11	02 25 15.2	+61 19 14.4	133.94	0.47	54.0	39	3
W4-I12	02 35 20.6	+62 16 02.3	134.70	1.79	52.5	77	2
W4-I13	02 28 25.1	+60 56 20.2	134.44	0.25	43.5	16	6
W4-I14	02 36 19.2	+61 44 05.5	135.01	1.35	31.4	2	16
W4-I15	02 33 36.1	+60 37 40.4	135.14	0.20	49.8	27	4
W4-I16	02 36 56.8	+61 57 58.6	134.99	1.59	43.3	35	0
W4-I17	02 34 08.8	+61 40 35.5	134.80	1.19	17.1	9	16
W4-I18	02 31 56.3	+61 25 50.9	134.65	0.87	5.6	24	2
W4-I19 ^c	02 40 31.7	+61 13 45.9	135.68	1.09	57.8	11	3
W4-I20	02 27 03.9	+61 52 24.9	133.94	1.07	47.6	457	0
W4-I21	02 30 44.5	+61 05 30.2	134.64	0.50	25.9	5	7
W4-I22 ^b	02 26 07.8	+61 56 43.7	133.82	1.09	55.4	—	—
W4-I23	02 40 30.9	+61 47 10.1	135.45	1.59	59.3	3	0
W4-I24	02 37 45.1	+60 37 31.4	135.61	0.40	61.5	20	10
W4-O1	02 41 33.9	+61 26 29.5	135.70	1.33	63.5	377	0
W4-O2	02 35 37.8	+59 56 29.5	135.64	-0.33	93.0	107	0
W4-O4	02 44 57.7	+62 28 06.5	135.64	2.43	105.8	747	0
W4-O5	02 21 52.6	+60 10 03.2	133.96	-0.75	110.3	94	0
W4-O6	02 31 59.2	+62 50 34.1	134.12	2.18	83.7	120	4
W4-O7	02 43 35.6	+61 55 54.6	135.72	1.88	82.7	52	0
W4-O8	02 23 04.5	+60 58 19.6	133.82	0.05	75.2	40	0
W4-O10	02 20 26.2	+61 34 46.2	133.31	0.51	88.0	64	3

^a Angular distance between the line of sight and a line of sight through the center of the star cluster.

^b NVSS position. No source detected in the Stokes I map in any frequency bin.

^c High Mass X-Ray Binary LSI +61°303.

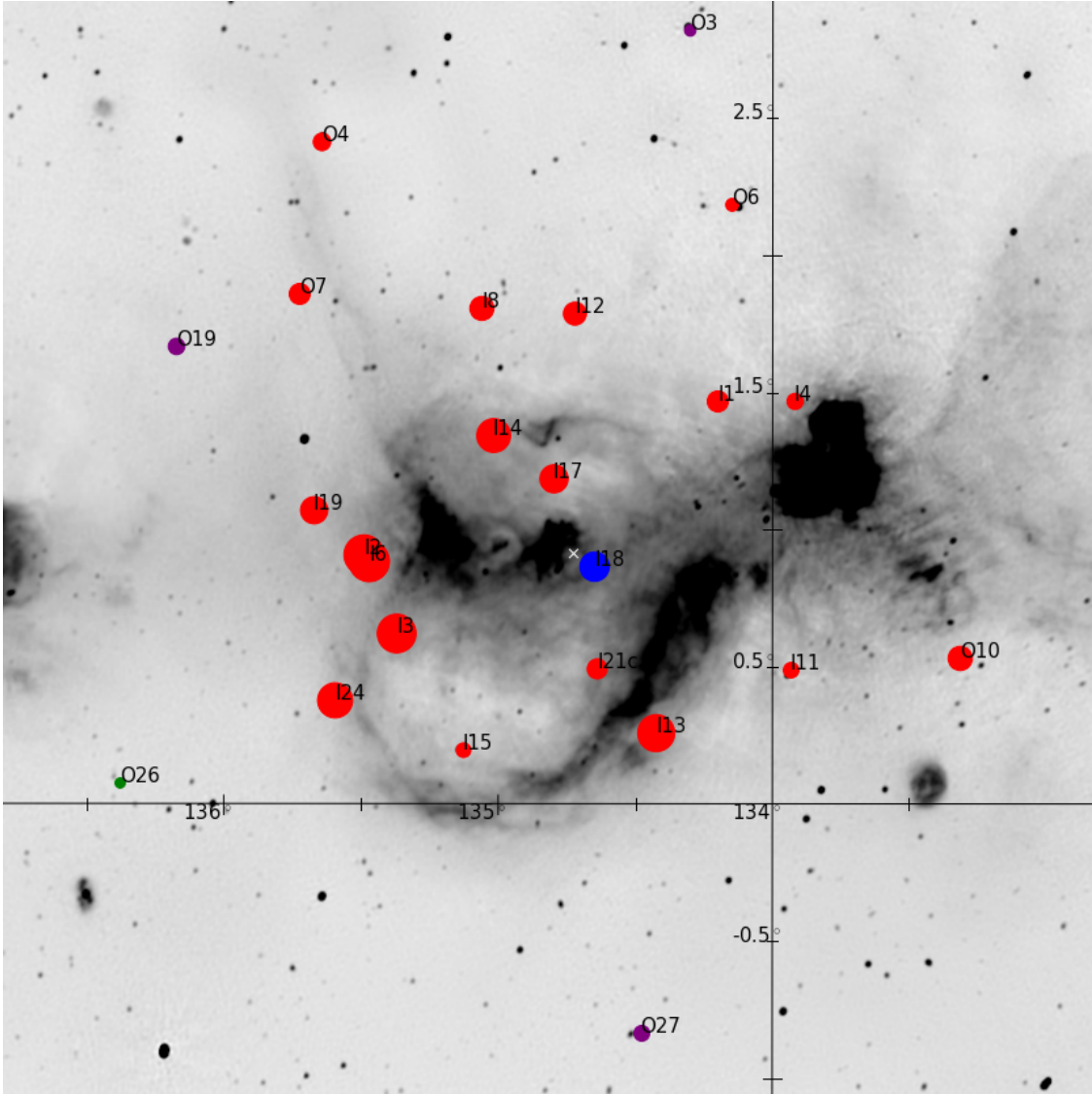


Fig. 2.— Mosaic of IC 1805 from the Canadian Galactic Plane Survey at 1.42 GHz, with Galactic longitude and latitude axes. The lines of sight listed in Table 1 are the red and blue symbols, where positive RMs are blue and negative RMs are red. The green and purple symbols are RM values from Taylor et al. (2009) or Brown et al. (2003), where positive RMs are green and negative RMs are purple. We utilize the naming scheme from Table 1 for the RM values from the literature for ease of reference, but we omit the “W4-” prefix in this image for clarity. The size of the plotted symbols is proportional to the $|RM|$ value.

Table 2: Log of Observations

VLA Project Code	13A-035
Date of Observations	2013 July 10, 13, 16, and 17
Number of Scheduling Blocks	4
Duration of Scheduling Blocks (h)	4
Frequencies of Observation ^a (GHz)	4.850; 7.250
Number of Frequency Channels per IF	512
Channel Width (MHz)	2
VLA array	C
Restoring Beam (diameter)	4''81
Total Integration Time per Source	18–25 minutes ^b
RMS Noise in Q and U Maps (μ Jy/beam)	39 ^c
RMS Noise in RM Synthesis Maps (μ Jy/beam)	23 ^d

^a The observations had 1.024 GHz wide intermediate frequency bands (IFs) centered on the frequencies listed, each composed of eight 128 MHz wide subbands.

^b The “O” sources (see Table 1) averaged 18 minutes, and the “I” sources, being weaker, were between 22–25 minutes.

^c This number represents the average rms noise level for all the Q and U maps.

^d Polarized sensitivity of the combined RM Synthesis maps.

2.2. VLA Observations

We observed 32 radio sources with the NSF’s Karl G. Jansky Very Large Array (VLA)¹ whose lines of sight pass through or near to the shell of the IC 1805 stellar bubble. Table 2 lists details of the observations. Traditionally, polarization observations require observing a polarization calibrator source frequently over the course of an observation to acquire at least 60° of parallactic angle coverage. This is done to determine the instrumental polarization (D-factors, leakage solutions). Since the completion of the upgraded VLA, shorter scheduling blocks, typically less than 4 hours in duration, have become a common mode of observation. It is difficult, if not impossible, with very short scheduling blocks to acquire enough parallactic angle coverage to measure the instrumental calibration with a polarized source. Another method of determining the instrumental polarization is to observe a single scan of an unpolarized source. This technique can be used with shorter scheduling blocks.

In this project we calibrated the instrumental polarization using both techniques. We used the source J0228+6721, observed over a wide range of parallactic angle, and also made a single scan of

¹The Karl G. Jansky Very Large Array is an instrument of the National Radio Astronomy Observatory (NRAO). The NRAO is a facility of the National Science Foundation, operated under cooperative agreement with Associated Universities, Inc.

the unpolarized source 3C84. Use of the CASA task POLCAL on the J0228+6721 data solved for the instrumental polarization, determined by the antenna-specific D factors (Bignell 1982), which are complex, as well as the source polarization (Q and U fluxes). In the case of 3C84, POLCAL solves only for the D factors. We find no significant deviations between these two calibration methods, indicating accurate values for the instrumental polarization parameters.

3C138 and 3C48 functioned as both flux density and polarization position angle calibrators. J0228+6721 was used to determine the complex gain of the antennas as a function of time as well to as serve as a check, as described above, for the D-factors. We observed the program sources for 5 minute intervals and interleaved the observations of J0228+6721. There was one observation of 3C138, 3C48, and 3C84 each. For our final data products, we utilized 3C84 as the primary leakage calibrator and 3C138 as the flux density and polarization position angle calibrator.

3. Data Reduction

The data were reduced and imaged using the NRAO Common Astronomy Software Applications (CASA)² version 4.5. The procedure for the data reduction as described in Section 3 of Costa et al. (2016) is identical to the procedure we employed in this study. The only difference for the current data set is that in the CASA task CLEAN, we utilized *Briggs* weighting with the “robust” parameter set to 0.5, which adjusts the weighting to be slightly more *natural* than *uniform*. *Natural* weighting has the best signal/noise ratio at the expense of resolution, while *uniform* is the opposite. *Briggs* weighting allows for intermediate options. As in our previous work, we also implemented a cutoff in the (u, v) plane for distances < 5000 wavelengths to remove foreground nebular emission.

Similar to Costa et al. (2016), we had two sets of data products after calibration and imaging. The first set of images consisted of radio maps (see Figures 3a and 3b) of each Stokes parameter, formed over a 128 MHz wide subband for each source. These images were inputs to the $\chi(\lambda^2)$ analysis (Section 3.1), and there were typically 14 individual maps for each source per Stokes parameter.

The second set of images consisted of maps of I , Q , and U in 4 MHz wide steps across the entire bandwidth using the CLEAN mode “channel”, which averages two adjacent 2 MHz channels. Ideally, changes in Q and U should only be due to Faraday rotation; however, the spectral index can affect Q and U independently of the RM, which can be interpreted as depolarization. RM Synthesis does not, by default, account for the spectral index, so a correction must be applied prior to performing RM Synthesis (see Section 3 of Brentjens & de Bruyn 2005). We first determine the spectral index, α , of each source from a least-squares fit to the log of the flux density, S_ν , and the log of the frequency, ν . We adopt the convention that $S_\nu \sim \nu^{-\alpha}$. We use the center frequency, ν_c ,

²For further reference on data reduction, see the NRAO Jansky VLA tutorial “EVLA Continuum Tutorial 3C391” (<http://casaguides.nrao.edu/index.php?title=EVLA-Continuum-Tutorial-3C391>)

of the band and the measured value of Q and U at each frequency, ν , to find Q_o and U_o using the relationship

$$Q = Q_o \left(\frac{\nu}{\nu_c} \right)^{-\alpha} \quad \text{and} \quad U = U_o \left(\frac{\nu}{\nu_c} \right)^{-\alpha}.$$

The final images consisted of approximately 336 maps per source, per Stokes parameter, as inputs for the RM Synthesis analysis (Section 3.2).

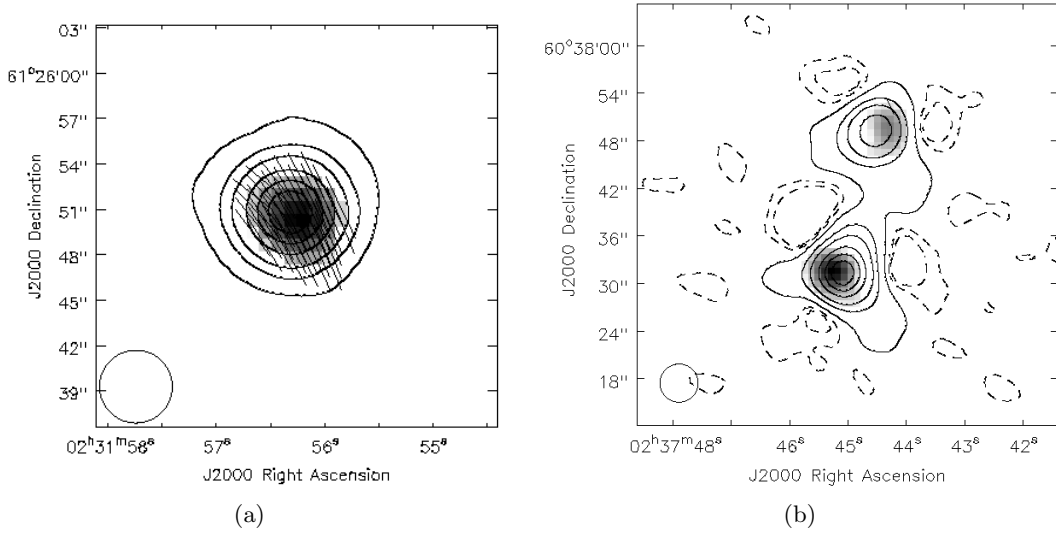


Fig. 3.— Map of (a) W4-I118 and (b) W4-I24 at 4913 MHz. The circle in the lower left is the restoring beam. The gray scale is the linear polarized intensity, P , the vectors show the polarization position angle, χ , and the contours are the Stokes I intensity with levels of -2, -1, 2, 10, 20, 40, 60, and 80% of the peak intensity, $21.5 \text{ mJy beam}^{-1}$ and $11.7 \text{ mJy beam}^{-1}$ for W4-I18 and W4-I24a, respectively.

3.1. Rotation Measure Analysis via a Least-Squares Fit to χ vs λ^2

The output of the CASA task CLEAN produces images in Stokes I , Q , U , and V . From these images, we generated maps with the task IMMATH of the linear polarized intensity P ,

$$P = \sqrt{Q^2 + U^2}$$

and the polarization position angle χ ,

$$\chi = \frac{1}{2} \tan^{-1} \left(\frac{U}{Q} \right)$$

for each source over a 128 MHz subband. Data that are below the threshold of $5\sigma_Q$ are masked in the P and χ maps, where $\sigma_Q = \sigma_U$ is the rms noise in the Q data. This threshold prevents noise

in the Q and U data from generating false structure in the P and χ maps. Examples of images are shown in Figure 3, which displays the total intensity, polarized intensity, and polarization position angle for sources W4-I18 and W4-I24. W4-I18 is an example of a point source, or slightly resolved source. Twelve of the sources in Table 1 were of this type and unresolved to the VLA in C array. Eight sources were like W4-I24, showing extended structure in the observations and potentially yielding RM values on more than one line of sight.

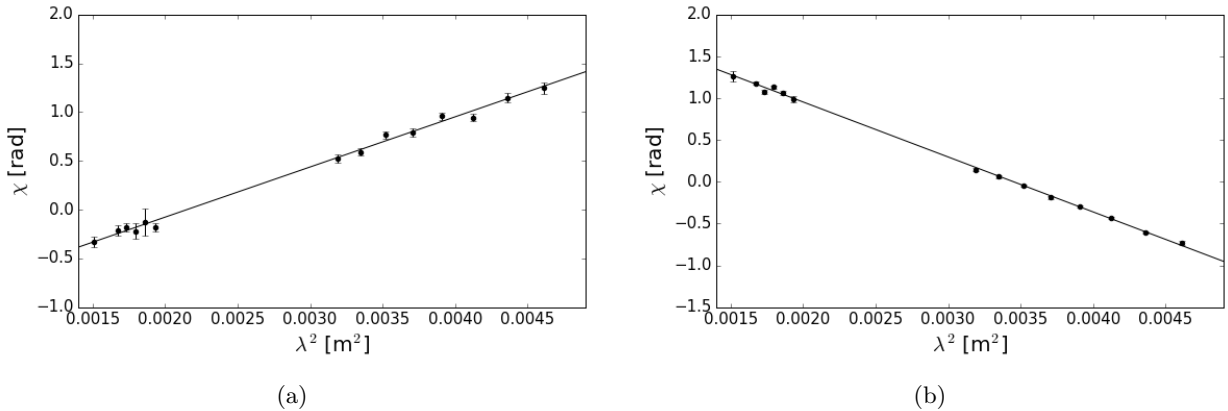


Fig. 4.— Plot of the polarization position angle as a function of the square of the wavelength, $\chi(\lambda^2)$, for the source (a) W4-I18, $\text{RM} = +514 \pm 12 \text{ rad m}^{-2}$, and (b) W4-I24a, $\text{RM} = -658 \pm 5 \text{ rad m}^{-2}$. Each plotted point results from a measurement in a single 128 MHz-wide subband. The gap in λ^2 coverage is due to the observation configuration that consisted of two 1.024 GHz wide IFs separated by $\sim 1.4 \text{ GHz}$.

In the case of a single foreground magnetic-ionic medium responsible for the rotation of an incoming radio wave, the relation between χ and λ^2 is linear, and we calculate the RM through a least-squares fit of $\chi(\lambda^2)$. To measure χ , we select the pixel that corresponds to the highest value of P on the source in the 4338 MHz map, and we then measure χ at that location in each subsequent 128 MHz wide subband. Figure 4 shows two examples of the least-squares fit to $\chi(\lambda^2)$. The χ errors are $\sigma_\chi = \frac{\sigma_Q}{2P}$, (Everett & Weisberg 2001, Equation 12).

3.2. Rotation Measure Synthesis

In addition to the least-squares fit to $\chi(\lambda^2)$, we performed Rotation Measure Synthesis (Brentjens & de Bruyn 2005). The inputs to RM Synthesis are images in Stokes I , Q , and U across the entire observed spectrum in 4 MHz spectral intervals. We refer the reader to Section 3.1.2 of Costa et al. (2016) for a detailed account of our procedure, which follows the implementation of RM Synthesis as developed by Brentjens & de Bruyn (2005). The goal of RM synthesis is to recover the Faraday dispersion function $F(\phi)$. Here ϕ , the Faraday depth, is a variable which is Fourier-conjugate to λ^2 (see Costa et al. 2016, Equations 3 and 4), and has units of rad m^{-2} . We also refer

to $F(\phi)$ as the “Faraday spectrum”.

Table 3: Rotation Measure Synthesis Parameters

$\Delta\lambda^2$	3.2×10^{-3} (m ²)	Total bandwidth ^a
λ_{min}^2	1.5×10^{-3} (m ²)	Shortest observed wavelength squared.
$\delta\lambda^2$	4.8×10^{-6} (m ²)	Width of a channel; Eq (35) Brentjens & de Bruyn (2005).
$\delta\phi$	1072 ^b (rad m ⁻²)	FWHM of RMSF; Eq (61) Brentjens & de Bruyn (2005).
max-scale	2098 (rad m ⁻²)	Sensitivity to extended Faraday structures; Eq (62) Brentjens & de Bruyn (2005).
$ \phi_{max} $	3.6×10^5 (rad m ⁻²)	Maximum detectable Faraday depth before bandwidth depolarization; Eq (63) Brentjens & de Bruyn (2005).

^a This bandwidth includes the frequencies not observed that lie between our two IFs. They are set to 0 via the weighting function, $W(\lambda^2)$.

^b Since flagging for RFI and bad antennas were done individually for each scheduling block, the FWHM of the RMSF can vary slightly from source to source. However, these slight variations are not significant in our interpretation of the RM values report in this paper.

$F(\phi)$ is recovered via an RMCLEAN algorithm (Heald 2009; Bell & Enßlin 2012), and we applied a 7σ cutoff, which is above the amplitude at which peaks due to noise are likely to arise (Brentjens & de Bruyn 2005; Macquart et al. 2012; Anderson et al. 2015). The RMSYNTHESIS algorithm initially searched for peaks in the Faraday spectrum using a range of $\phi \pm 10,000$ rad m⁻² at a resolution of 40 rad m⁻² to determine if there were significant peaks at large values of $|\phi|$. Then, we performed a finer search at $\phi = \pm 3000$ rad m⁻² at a resolution of 10 rad m⁻². The RM Synthesis parameters, such as the full-width-at-half-maximum (FWHM) of the rotation measure spread function (RMSF) and the maximum detectable Faraday depth, are given in Table 3.

As in Costa et al. (2016), we utilized an IDL code for the RMSYNTHESIS and RMCLEAN algorithms. The output of the IDL code is a data cube in Faraday depth space that is equal in range to the range of ϕ that was searched over in the RMSYNTHESIS algorithm. The data cube contains, for example, 500 maps of the polarized intensity as a function of spatial coordinates and ϕ , which ranges between $\pm 10,000$ rad m⁻² at intervals of 40 rad m⁻². Initially, we generated these maps for a 1024×1024 pixel image. We then used the Karma package (Gooch 1995) tool KVIS to review the maps to search for sources or source components away from the phase center that, while being too weak to detect in the 128 MHz maps, may be detectable in the RM Synthesis technique since it uses the entire bandwidth to determine the Faraday spectrum³. However, no such sources were identified above the cutoff. From the 1024×1024 maps of the Faraday spectrum, we identified

³private communication, L. Rudnick

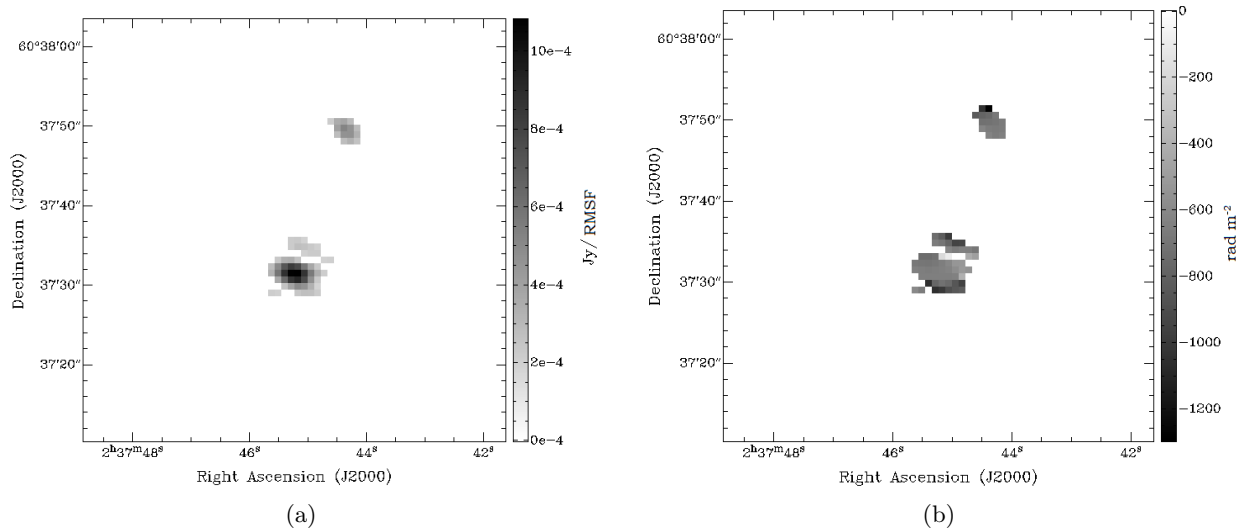


Fig. 5.— (a) Linear polarization map and (b) RM map of W4-I24 from the RM Synthesis analysis. In both images, the data cube was flattened over the Faraday depth axes, and a threshold of 7σ was applied. W4-I24 has extended structure, so there are two peaks, which are also present in the CASA maps (Figure 3b).

the P_{max} for the observed sources and extracted the Faraday spectrum at that location. Figure 5a shows an example of a P_{max} map that has been flattened along the ϕ axis, i.e., the gray scale in the image represents the full range of ϕ . From this map, it is easy to identify the spatial location of P_{max} for the source, which agrees with the location of the peak linear polarized intensity in the $\chi(\lambda^2)$ analysis. We obtained this same result in Costa et al. (2016) for the Rosette Nebula.

To determine the RM, we fit a 2 degree polynomial to the Faraday spectrum at each pixel in the 1024×1024 image above the 7σ cutoff. The gray scale in Figure 5b shows the RM value from the fit to each pixel. The image is zoomed and centered on the source. While we can mathematically determine the RM at each pixel, the sources are not resolved, so we only select the RM at the spatial location of P_{max} . Figure 6a plots the Faraday spectrum and RMCLEAN components for W4-I18, and Figure 6b shows the RMSF.

Anderson et al. (2015) describe two cases for the behavior of the Faraday spectrum. A source is considered *Faraday simple* when $F(\phi)$ is non-zero at only one value of ϕ , Q and U as a function of λ^2 vary sinusoidally with equal amplitude, and $P(\lambda^2)$ is constant. The *Faraday simple* case has the physical meaning of a uniform Faraday screen in the foreground that is responsible for the Faraday rotation, and χ is linearly dependent on λ^2 . If a source is *Faraday simple*, then $F(\phi)$ is a delta function at a Faraday depth equal to the RM. The second behavior Anderson et al. (2015) describe for the Faraday spectrum is a *Faraday complex* source, which is any spectrum that deviates from the criteria set for the *Faraday simple* case. A *Faraday complex* spectrum can be the result of depolarization in form of beam depolarization, internal Faraday dispersion, multiple interfering

Faraday rotating components, etc. (Sokoloff et al. 1998).

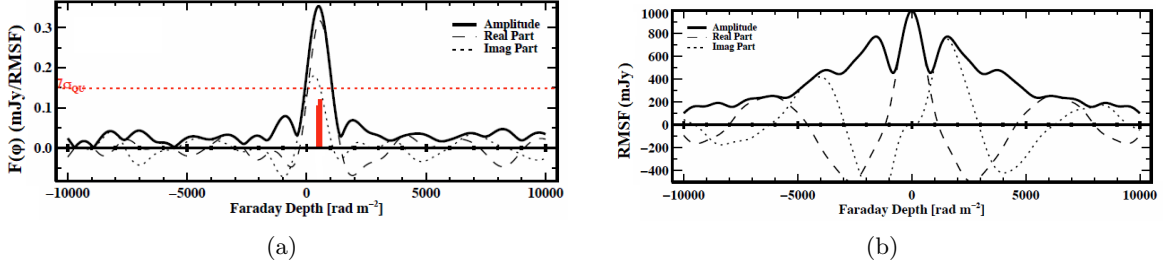


Fig. 6.— Plot of (a) cleaned Faraday dispersion function, $F(\phi)$, for W4-I18, where $\phi_{peak} = 501 \pm 33 \text{ rad m}^{-2}$ and (b) the RMSF ($R(\phi)$). The 7σ cutoff is shown in the red, dashed, horizontal line. The vertical red lines are the clean components, and the black curves represent the P (solid), Q (dot dashed), and U (dashed) components of the spectrum.

4. Observational Results

4.1. Measurements of Radio Sources Viewed Through the W4 Complex

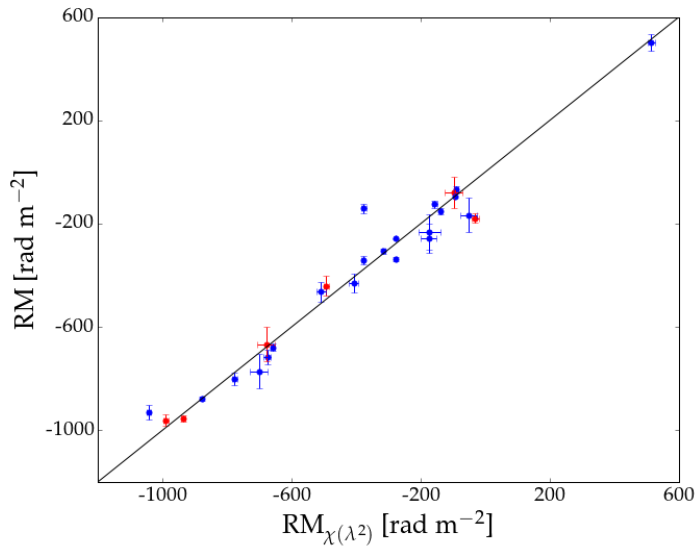


Fig. 7.— Plot of RM values derived from the $\chi(\lambda^2)$ analysis vs the RM Synthesis analysis. The blue markers are the RM from primary component and the red are the secondary component. The straight line represents perfect agreement between the two sets of measurements.

We measured 27 RM values for 20 lines of sight, including secondary components, through or

near to IC 1805. In Table 4, the first column lists the source name using our naming scheme, and column two gives the component, if the source had multiple resolved components for which we could determine a RM value. Columns three and four list the RM value from the least-squares method and the reduced chi-squared value, respectively. Column five lists the RM value determined from the RM Synthesis technique and the associated error (Equation 7 of Mao et al. 2010).

Figure 7 shows the agreement between the two techniques for determining the RM. As in Costa et al. (2016), we find good agreement between the two techniques, and the good agreement between the results using the two techniques gives us confidence in our RM measurements.

4.2. Report on Faraday Complexity and Unpolarized Lines of Sight

In the last paragraph of Section 3.2, we discuss Faraday complexity. If a source is *Faraday simple*, then the RM is equal to a delta function in $F(\phi)$ at the Faraday depth. If a source is *Faraday complex*, then the interpretation of the RM is not as straightforward. There is extensive literature (e.g. Farnsworth et al. 2011, O’Sullivan et al. 2012, Anderson et al. 2015, Sun et al. 2015, Purcell et al. 2015) to understand Faraday complexity.

One indicator of a *Faraday complex* source is a decreasing fractional polarization, $p = P/I$, as a function of λ^2 . The ways in which this can arise are discussed at the end of Section 3.2. Although depolarization does not necessarily lead to a net rotation of the source χ , its presence indicates the potential for a χ rotation independent of the plasma medium through which the radio waves subsequently propagate. This could result in an error in our deduced RMs. Nine of the sources, W4-I1, -I3, -I11, -I15, I21b, -O4, -O6, -O7, and -O10 show a decreasing p with increasing λ^2 .

A rough estimate of the potential position angle rotation associated with depolarization may be obtained using the analysis in Cioffi & Jones (1980). These calculations assume that depolarization arises from Faraday rotation within the synchrotron radiation source, and we can estimate the effect of internal depolarization from the changes in fraction polarization. Given the fractional polarization at the shortest and longest wavelength, we obtain the corresponding polarization angle change from Figure 1 of Cioffi & Jones (1980) and then calculate a RM due to internal depolarization. If the calculated RM due to depolarization (RM_{depol}) is larger than the observed RM, then the RM is potentially affected by depolarization. W4-I1, -O6, -O7, and -O10 show $RM_{depol} \sim RM_{obs}$, which indicates that internal depolarization could affect the observed RM. The observed RM of W4-I3 is ~ 3 times larger than RM_{depol} , so it is not affected by internal depolarization.

Depolarization due to internal Faraday rotation makes predictions for the form of $\chi(\lambda^2)$ which would not have $\chi \propto \lambda^2$ (Cioffi & Jones 1980). For all of the sources mentioned above, we compared the observed behavior of $\chi(\lambda^2)$ to the predicted behavior (Equation 4b of Cioffi & Jones 1980). Within the errors, only W4-O7 is consistent with the non-linear behavior of a RM affected by internal depolarization. We interpret this result as meaning that our deduced RM values for most of the sources are not significantly in error due to internal depolarization, and we consider the

Table 4: Faraday Rotation Measurement Values through the W4 Complex

Source	Component	RM ^a (rad m ⁻²)	Reduced χ^{2b}	RM ^c (rad m ⁻²)	ξ^d (pc)	ξ^e (pc)
W4-I1	a	-277 ± 1	29	-258 ± 3	29	53
W4-I2	a	-1042 ± 7	1.5	-930 ± 30	30	26
	b	-935 ± 6	1.5	-954 ± 11		
W4-I3	a	-876 ± 2	1.9	-878 ± 8	27	16
W4-I4	a	-139 ± 3	1.9	-153 ± 12	38	59
	b	-91 ± 6	2	-68 ± 15		
W4-I6	a	-990 ± 8	1.3	-961 ± 23	29	25
W4-I8	a	-276 ± 2	4.4	-337 ± 8	37	54
W4-I11	a	-377 ± 8	12	-141 ± 18	35	41
W4-I12	a	-315 ± 4	2.8	-306 ± 10	34	54
W4-I13	a	-777 ± 8	1.2	-801 ± 24	28	36
	b	-701 ± 28	0.5	-772 ± 66		
W4-I14	a	-678 ± 27	0.6	-666 ± 66	20	36
W4-I15	a	-157 ± 9	0.8	-124 ± 14	32	10
W4-I17	a	-492 ± 8	1.6	-440 ± 40	11	31
	b	-509 ± 15	0.6	-464 ± 40		
W4-I18	a	+514 ± 12	1.1	+501 ± 33	4	22
W4-I19	a	-407 ± 14	0.3	-431 ± 36	37	34
W4-I21	a	-53 ± 26	1.4	-167 ± 67	17	15
	b	-98 ± 28	0.5	-79 ± 62		
	c	-173 ± 34	0.5	-232 ± 70		
W4-I24	a	-658 ± 5	1.4	-678 ± 14	39	23
	b	-675 ± 12	0.4	-716 ± 30		
W4-O4	a	-31 ± 12	24	-178 ± 18	68	81
W4-O6	a	-95 ± 1	3.6	-96 ± 4	54	76
W4-O7	a	-175 ± 24	0.8	-256 ± 56	53	62
W4-O10	a	-379 ± 5	1.8	-343 ± 16	56	66

^a RM value obtained from a least-squares linear fit to $\chi(\lambda^2)$. The errors are 1σ .

^b Reduced χ^2 for the $\chi(\lambda^2)$ fit.

^c Effective RM derived from RM Synthesis.

^d Distance from center of OCl 352.

^e Distance from Terebey et al. (2003) center.

measurement of depolarization as providing a cautionary flag.

We also considered whether our measurements could have been affected by bandwidth depolarization or beam depolarization. Bandwidth depolarization occurs when the polarization angle varies over frequency averaged bins, $\Delta\nu$. For example in this study, we use values of χ in 128 MHz wide bins (Section 3.1) and 4 MHz (Section 3.2). For a center frequency of the lowest frequency bin, we use $\nu_c = 4466$ MHz, and the relationship between the change in polarization position angle, $\Delta\chi$, is

$$|\Delta\chi| = 2|\text{RM}| c^2 \frac{\Delta\nu}{\nu_c^3}, \quad (3)$$

where c is the speed of light. This formula shows that even for $|\text{RM}| = 10^4$ rad m⁻², which is far larger than any RMs we measure, the Faraday rotation across the band is 0.41 radians. This is insufficient to cause substantial bandwidth depolarization. Beam depolarization occurs when there are small scale variations of the electron density or the magnetic field within a beam. It is unlikely that the RMs are affected by beam depolarization as the beam at 6 cm for the VLA in C array is ~ 5 arcseconds. We interpret these RMs as a characteristic value due to the plasma medium (primarily the Galactic ISM) between the source and the observer. In the analysis that follows, we choose the RM values from the RM Synthesis method.

When the data were mapped and inspected, we found that a few sources that had passed our criteria for flux density and compactness to the VLA D array at L band (1.42 GHz) were completely unpolarized. W4-I16 and W4-O8 are not polarized at any frequency, and the RM Synthesis technique does not show significant ($> 7\sigma$) peaks at any ϕ . Three of the lines of sight, W4-I5, W4-I10, and W4-I22, have no source in the field. Despite appearing to be point sources in the NVSS postage stamps (see Section 2), we do not observe a source at these locations, and they may have been clumpy foreground nebular emission that was filtered out during the imaging process.

Subsequent investigations determined that some of the selected sources were previously cataloged ultra compact H II regions associated with the W3 star formation region. These sources are W4-I7 (W3(OH)-C), W4-I9 (AFGL 333), and W4-I20 (W3(OH)-A) (Feigelson & Townsley 2008; Navarete et al. 2011; Román-Zúñiga et al. 2015). The W4-I7 field has no source at the observed α and δ , despite it being identified as W3(OH)-C. We do not observe a source at this location in any frequency bin. W3(OH)-A, however, is observed and is a point source in our maps at all frequencies. Similarly, W4-I9 is detected in each frequency bin and is an extended source. These sources are unpolarized and do not feature in our subsequent analysis.

4.3. A Unique Line of Sight Through the W4 Region: LSI +61°303

W4-I19 has a spectrum which is inconsistent with an optically-thin extragalactic radio source. It is linearly polarized, and we measure $\text{RM} = -431 \pm 36$ rad m⁻². Investigation of this source

during the data analysis phase revealed that it is not an extragalactic source, although it passed our selection criteria for flux and compactness. W4-I19 is the high mass X-ray binary (HMXB) LSI +61°303 (Gregory et al. 1979; Bignami et al. 1981), which is notable for being one of five known gamma ray binary systems (Frail & Hjellming 1991). This system has been extensively studied, and as a result, much is known about the nature of the compact object (Massi et al. 2004; Massi 2004; Dubus 2006; Paredes et al. 2007; Massi et al. 2017), the stellar companion (Casares et al. 2005; Dubus 2006; Paredes et al. 2007), orbital period (Gregory & Neish 2002), radio structure (Albert et al. 2008), and radial velocity (Gregory et al. 1979; Lestrade et al. 1999).

The spatial location of LSI +61°303 is important for understanding the RM we determined for this source. Frail & Hjellming (1991) argue that since signatures of the Perseus arm shock are present in the absorption spectrum to LSI +61°303 but not the post-shock gas from the Perseus arm, LSI +61°303 must lie between the two features at a distance of 2.0 ± 0.2 kpc. They also report that they do not see absorption features due to the IC 1805 ionization front and shock front. The estimated distance to LSI +61°303 is consistent with distance estimates to OCl 352. The position relative to the nebula has consequences for the interpretation of the RM that we measure. The possibilities are:

1. LSI +61°303 is in front of the stellar bubble and H II region, so it is exterior to a region modified by OCl 352. The RM is then an estimate of the foreground ISM between us and the nebula.
2. If LSI +61°303 is at the same distance as IC 1805 or slightly behind (greater distance), then the RM is unique among our sources in that it is not affected by Faraday rotation from material in the outer Galaxy. The RM is then probing at least a part of the Faraday rotating material due to the nebula.

To further determine the position of LSI +61°303 with respect to IC 1805, we review the current state of knowledge on the subject from the literature. Dhawan et al. (2006) observed LSI +61°303 with the Very Long Baseline Array (VLBA) and report a proper motion of $(\mu_\alpha, \mu_\delta) = (-0.30 \pm 0.07, -0.26 \pm 0.05)$ mas yr⁻¹. Aragona et al. (2009) report a radial velocity for LSI +61°303 of $V_{rad} = -41.4 \pm 0.6$ km s⁻¹, which agrees with previous estimates by Casares et al. (2005). For OCl 352, Dambis et al. (2001) estimate the radial velocity to be -41 ± 3 km s⁻¹, and more recent estimates by Kharchenko et al. (2005) ($V_{rad} = -47 \pm 18$ km s⁻¹) agree within the errors. Both LSI +61°303 and OCl 352 have similar radial velocities, and the proper motion estimates by Dhawan et al. (2006) indicate that LSI +61°303 is moving similarly on the plane of the sky to OCl 352, which has a proper motion of $(\mu_\alpha, \mu_\delta) = (-1.0 \pm 0.4, -0.9 \pm 0.4)$ mas yr⁻¹ (Dambis et al. 2001).

From proper motion and radial velocity estimates, LSI +61°303 appears to be moving in relatively the same direction and speed as OCl 352. Using a distance of 2 kpc to LSI +61°303 and 2.2 kpc to OCl 352, the transverse velocities are ~ 3 km s⁻¹ and ~ 14 km s⁻¹, respectively. If LSI

+61°303 originally belonged to OCl 352, then it is unlikely that it is in front of IC 1805, given that both are moving at the same radial velocity. While LSI +61°303 appears to be outside the obvious shell structure of IC 1805, it is more likely that it is probing material modified by OCl 352. We discuss this possibility further in Section 5.3.

If LSI +61°303 did not originate in OCl 352, then it is possible to still be in front of the nebula, despite the similar velocities. In such a case, the RM we obtained for this line of sight is due to the ISM between us and IC 1805. The RM value we find for LSI +61°303 is nearly 3 times larger than the background RM, which we discuss in Section 5.2. This would require a magneto-ionic medium between the observer and the nebula capable of producing $\sim 400 \text{ rad m}^{-2}$ along this line of sight. As may be seen from Table 4 and Figure 2, other lines of sight near IC 1805, but exterior to the shell, do not have as large of RM values (e.g. W4-O26, -O19, -O7, -I11). It therefore seems most probable that the RM for W-I19 (LSI +61°303) is dominated by plasma in W4.

In summary, there is evidence in the literature that suggests LSI +61°303 may lie within a region modified by OCl 352, particularly if LSI +61°303 did indeed once belong to OCl 352. If this is the case, then the RM we find is unaffected by the ISM in the outer galaxy and is due to the material near IC 1805.

5. Results on Faraday Rotation Through the W4 Complex

5.1. The Rotation Measure Sky in the Direction of W4

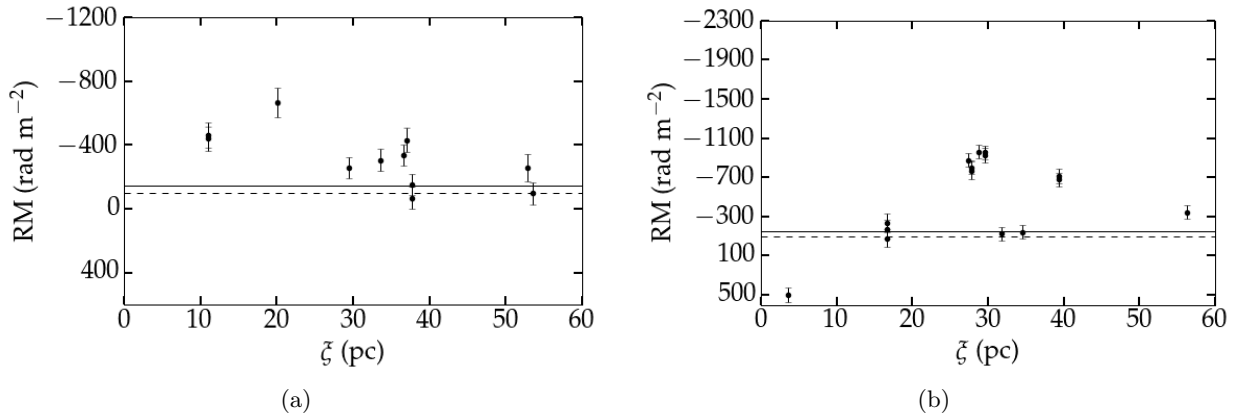


Fig. 8.— Plot of RM vs distance from the center of OCl 352 for (a) lines of sight that pass through the W4 Superbubble and (b) lines of sight near and close to the southern loop. The solid line represents the estimate of the background RM using sources in this study and in the literature, and the dashed line is the predicted background RM from the Van Eck et al. (2011) model of the Galactic magnetic field.

Whiting et al. (2009), Savage et al. (2013), and Costa et al. (2016) compared observations to a model of the ionized shell in which the RM depended only on ξ , the impact parameter, or closest approach of a line of sight to the center of the shell. In anticipation of a similar analysis in this study, we show Figures 8a and 8b, which plot the RM versus distance from the center of star cluster for the lines of sight through the W4 Superbubble (W4-I1, -I4, -I8, -I12, -I14, -I17, -O4, -O6, and -O7) and the ones through or close to the southern loop (W4-I2, -I3, -I6, -I11, -I13, -I15, -I18, -I19, -I21, -I24, -O10).

In Section 1.2, we discussed the morphology of the region around IC 1805 and made the distinction between the southern latitudes and the northern latitudes, so in the following sections, we address each region near IC 1805 separately.

5.2. The Galactic Background RM in the Direction of W4

In Savage et al. (2013), we determined the background RM in the vicinity of the Rosette Nebula ($\ell \sim 206^\circ$) by finding the median value of the RM for sources outside the obvious shell structure of the Rosette. Determining the background RM near IC 1805 is difficult, however, due to proximity of W3, the W3 molecular cloud, and the W4 Superbubble. Given the morphological difference between the northern and southern parts of IC 1805, we assume that sources south of OCl 352 ($b < 0.9^\circ$) should be modeled independently of the northern sources, since the W4 Superbubble extends up to $b \sim 7^\circ$ (West et al. 2007). The lines of sight north of the star cluster are intersecting the W4 Superbubble and are not probing the RM due to the general ISM independent of IC 1805. Therefore, the only lines of sight that are potentially probing the RM in the vicinity of IC 1805 are those exterior to the shell structure of the southern loop.

Table 5: List of Sources with RM values from Catalogs

Source Name	α (J2000) h m s	δ (J2000) ° ' "	RM ^a (rad m ²)
W4-O3	02 35 43.0	+63 22 33.0	$-138^b \pm 18$
W4-O19	02 46 23.9	+61 33 19.9	$-157^c \pm 15$
W4-O26	02 42 32.3	+60 02 31.0	$+61 \pm 41$
W4-O27	02 25 48.7	+59 53 52.0	-145 ± 22

^a RM values from Brown et al. (2003) unless otherwise noted.

^b Taylor et al. (2009) give -75 ± 9 rad m⁻² for this line of sight.

^c RM value from Taylor et al. (2009).

If we apply the thick shell model from Terebey et al. (2003) (see Section 1.2 for details), then the lines of sight with RM values exterior to the shell are W4-I2, -I11, and -O10. For the thin

shell case, W4-I6, -I13 and -I24 are also exterior sources. The mean RM value for the background using these sources is -554 rad m^{-2} and -670 rad m^{-2} for the thick or thin shell, respectively. In Table 5, we list RM values from the literature for lines of sight near IC 1805 that we include in our estimate of the background RM. The mean RM value for these sources (excluding W4-O3 for being in the superbubble) is -80 rad m^{-2} . The sources W4-I2, -I6, -I13, and -I24 are seemingly outside the obvious ionized shell structure; however, they are also the lines of sight for which we measure some of the highest RM values. This is a surprising result, and one we did not observe in the case of the Rosette Nebula. It strongly suggests that the lines of sight to W4-I2, -I6, -I13, and -I24 have RMs that are dominated by the W4 complex, despite the fact that they are outside the obvious ionized shell of IC 1805. We discuss this further in the next section.

For the present discussion, we exclude these sources from the estimate of the background. Using W4-I11, -O10, -O19, -O26, and -O27, we find a mean value for the background RM due to the ISM of -145 rad m^{-2} . While this value is similar in magnitude to the value of the background RM we found in our studies on the Rosette Nebula, we have significantly fewer lines of sight, and only two of the lines of sight were observed in this study.

Due to a low number of lines of sight exterior to IC 1805, we utilize the model of a Galactic magnetic field by Van Eck et al. (2011) to estimate the background RM due to the ISM. From their Figure 6, they find the Galactic magnetic field is best modeled by an almost purely azimuthal, clockwise field. Van Eck et al. (2011) use their model to predict the RM values in the Galaxy, and in the vicinity of IC 1805, their model predicts RMs of order -100 rad m^{-2} . Using this as an estimate of the background RM, we find an excess RM due to IC 1805 of $+600$ to -860 rad m^{-2} .

5.3. High Faraday Rotation Through Photodissociation Regions

The lines of sight with the highest RM values, W4-I2, -I6, and -I24, appear to be outside the obvious shell of the southern loop. These sources are very near to the bright ionized shell. Terebey et al. (2003) and Gray et al. (1999) discuss a halo of ionized gas that surrounds IC 1805, which may be causing the high RM values. Gray et al. (1999) speculate that the diffuse extended structure is an extended H II envelope as suggested by Anantharamaiah (1985). Another possibility is that these high RMs arise in the PDR surrounding the IC 1805 H II region.

PDRs are the regions between ionized gas, which is fully ionized by photons with $h\nu > 13.6 \text{ eV}$, and neutral or molecular material. PDRs can be partially ionized and heated by far-ultraviolet photons ($6 \text{ eV} < h\nu < 13.6 \text{ eV}$) (Tielens & Hollenbach 1985; Hollenbach & Tielens 1999). Typically, the PDR consists of neutral hydrogen, ionized carbon, and neutral oxygen nearest to the ionization front, and with increasing distance, molecular species (e.g., CO, H₂, and O₂) dominate the chemical composition of a PDR (Hollenbach & Tielens 1999). One tracer of PDRs is polycyclic aromatic hydrocarbon (PAH) emission at infrared (IR) wavelengths. Churchwell et al. (2006) identify more than 300 bubbles at IR wavelengths in the Galactic Legacy Infrared Mid-Plane Survey

Extraordinaire (GLIMPSE), and 25% of these bubbles coincide with known H II regions. Watson et al. (2008) examine three bubbles from the Churchwell et al. (2006) catalog with the *Spitzer* Infrared Array Camera (IRAC) bands 4.5, 5.8, and 8.0 μm and the 24 μm band from the *Spitzer* Multiband Imaging Photometer (MIPS) to determine the extent of the PDR around three young H II regions. One of their main results is that the 8 μm emission, which is due to PAHs, encloses the 24 μm emission, which traces hot dust. Kerton et al. (2013) discuss similar observations near the W 39 H II region. Watson et al. (2008) use ratios between the 4.5, 5.8, and 8.0 μm bands to determine the extent of the PDRs, as the 4.5 μm emission does not include PAHs but the 5.8 and 8.0 μm bands do (see their Section 1 for details).

To determine the presence and extend of a potential PDR around IC 1805, we analyze Wide-field Infrared Survey Explorer (WISE) data from the IPAC All-Sky Data Release⁴ at 3.6, 4.6, 12, and 22 μm . The 4.6 μm WISE bands is similar in bandwidth and center frequency to the IRAC 4.5 μm band, and the WISE 22 μm band is also similar to the MIPS 24 μm band (Anderson et al. 2014). The 12 μm WISE band does not overlap with the 8.0 μm band of IRAC, but the WISE band traces PAH emission at 11.2 and 12.7 μm . Anderson et al. (2012) note, however, that the 12 μm flux is on average lower than the 8.0 μm IRAC band, which is most likely due to the WISE band sampling different wavelengths of PAH emission instead of the 7.7 and 8.6 μm PAH emission in the IRAC band.

Figure 9 is a RGB image of the southern loop of IC 1805 at 4.6 μm (blue), 12 μm (green), and 22 μm (red). The 1.42 GHz radio continuum emission is shown in the white contours at 8.5, 9.5, and 10 K, and the lines of sight that intersect this region are labeled as well. Similar to the results of Watson et al. (2008), the majority of the 22 μm emission is located inside the bubble. The radio contours trace the ionized shell of the H II region, which show a patchy ionized shell. Outside of the radio contours, there is a shell of 12 μm (green) PAH emission that encloses the 22 μm emission as well. In the northeastern portion of the image, there is extended 22 μm (hot dust) emission, which is spatially coincident with a CO clump (Lagrois & Joncas 2009a).

The PDR model predicts the presence of neutral hydrogen and molecular CO (see Figure 3 of Hollenbach & Tielens 1999) at increasing distance from the exciting star cluster. Figure 1 of Sato (1990) and Figure 2 of Hasegawa et al. (1983) show H I contours in the vicinity of IC 1805, and the H I emission appears to completely enclose the southern loop except near $135.5^\circ \leq \ell \leq 136^\circ$, $0.2^\circ \leq b \leq 0.9^\circ$. Braunsfurth (1983) report H I emission near IC 1805, and he notes that the hole could be due to cold H I gas or the lack of gas if the winds have sufficiently swept the material away or ionized it. Figure 6 of Digel et al. (1996) shows the CO emission, with the W3 molecular cloud on the western side of IC 1805, CO emission along the southern loop of IC 1805, and the molecular material associated with the W5 ($\ell = 137.1$, $b = +0.89$) H II region on the eastern side of IC 1805. We interpret the WISE data, the radio contours, and the CO and H I maps as a patchy ionized shell surrounded by a PDR.

⁴<http://wise2.ipac.caltech.edu/docs/release/allsky/>

If there is a PDR surrounding IC 1805, then the highest RM values from our data set, RM = -954 rad m^{-2} and -961 rad m^{-2} for W4-I2 and -I6, respectively, lie outside the ionized shell of the H II region and in the PDR. Similarly, the sources W4-I19 and -I24 are also outside the radio continuum contours but appear to be within the $12 \mu\text{m}$ (green) emission. This is a surprising result compared with our results from the Rosette Nebula, where we found the highest RM values for lines of sight that pass through the ionized shell. Gray et al. (1999) note zones of depolarization near the southern portion of IC 1805, which require RMs on order 10^3 rad m^{-2} , and spatial RM gradients. The RMs for W4-I2 and -I6 are on this order, but those for W4-I24 and -I19 are not, and we do not find that these lines of sight are affected by depolarization. W4-I24 has two components for which we measure RMs, and the components are separated by ~ 18 arcseconds. The ΔRM , which is the difference in RM between the two components is 38 rad m^{-2} , which is not a large change in the RM and is consistent within the errors.

The presence of the PDR is complicated, however, by the extended diffuse ionized emission reported by Terebey et al. (2003) and Gray et al. (1999). At lower contours, the high RM sources do lie within the radio continuum emission. To fully understand the presence and extent of a PDR or an extended H II envelope, observations of radio recombination lines on the eastern side of IC 1805 would clarify the structure as well as observations of other tracers of PDRs (e.g., fine structure lines of C and C⁺, H₂, and CO). It may be the case that the ionized shell is patchy along the shell wall, which allows photons $> 13.6 \text{ eV}$ to escape the shell at places, but the shell is sufficiently ionization-bounded at other places such that a PDR can form.

5.4. Faraday Rotation Through the Cavity and Shell of the Stellar Bubble

There are four lines of sight through the cavity of the stellar bubble, assuming an inner radius from the Terebey et al. (2003) model. The sources W4-I3, -I15, -I18, and -I21 are through the cavity, and including multiple components, we find 6 RM values. W4-I3 has a high RM ($-878 \pm 18 \text{ rad m}^{-2}$), and W4-I15 and -I21 have comparatively low RM values (-79 to -232 rad m^{-2}). Examination of Figures 2 and 9 does not reveal enhanced emission near W4-I3 in comparison to W4-I21. W4-I15, however, is in a region of relatively low emission, which may explain why W4-I15 has a RM value at least 4 times smaller than W4-I3.

W4-I13 is outside the shell, assuming a shell radius from either Terebey et al. (2003) model. From Figure 2, it does appear to be outside the ionized shell. However W4-I13 is within a 8.5 K contour on the 1.42 GHz radio continuum map, which may indicate that it is probing the ionized shell. We find a high RM for both components of this source, which is similar to the RM values for W4-I2 and -I6.

Across IC 1805, we observe negative RM values for all lines of sight except one: W4-I18, which is 5.6 arcmin (4 pc) from the center of the star cluster. The absolute value of the RM for W4-I18 is also large ($+501 \pm 33 \text{ rad m}^{-2}$), indicating a large change in RM along this line of sight relative to

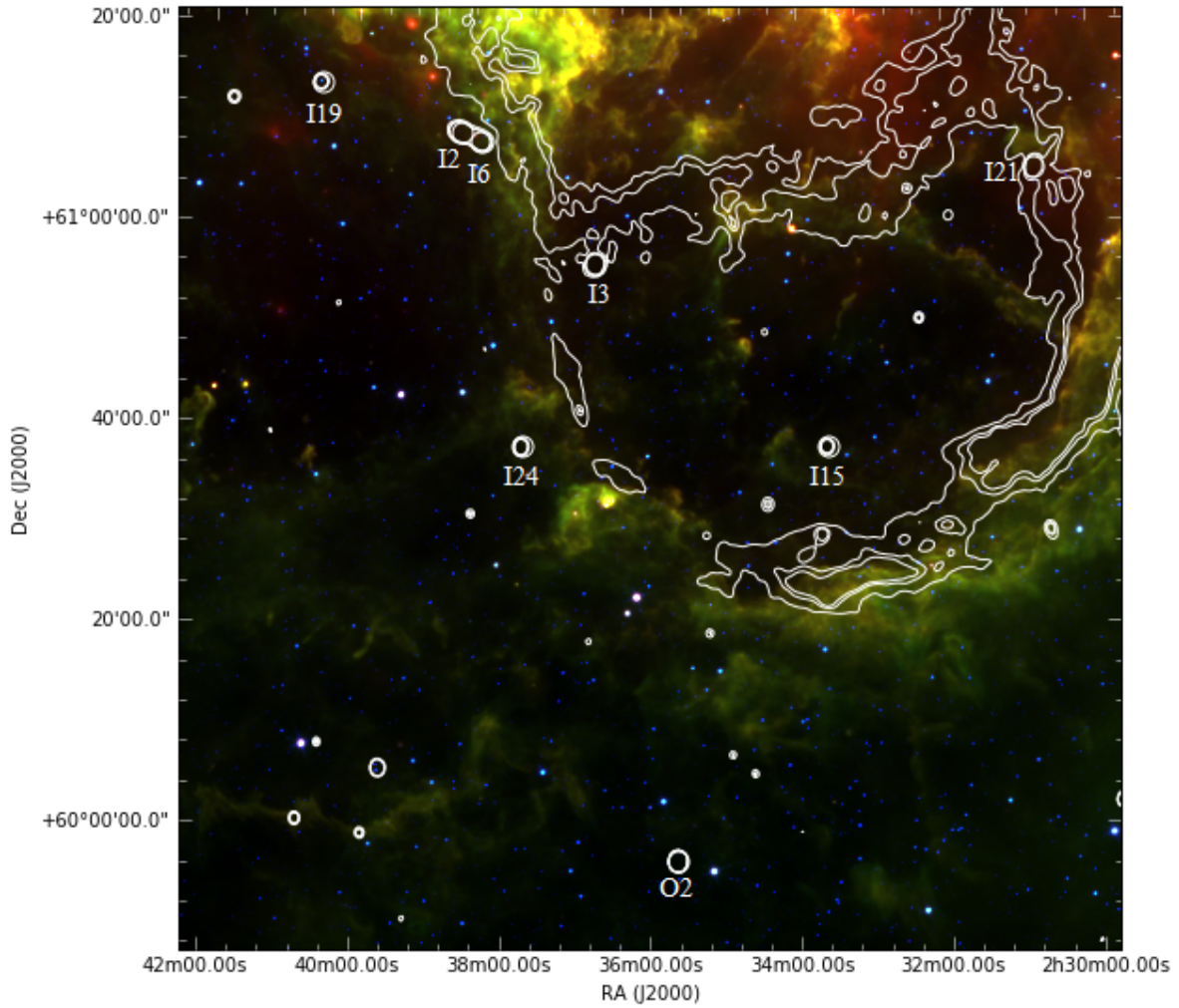


Fig. 9.— Inset from Figure 2. A RGB image of archive WISE data at $4.6 \mu\text{m}$ (blue), $12 \mu\text{m}$ (green), and $22 \mu\text{m}$ (red) with CGPS contours at 8.5, 9.5, and 10 K in white. The lines of sight from the present study are shown with circles and are labeled according to Table 1.

other lines of sight in this part of the sky. This line of sight is probing the space close to the massive O and B stars responsible for IC 1805. In the Weaver et al. (1977) model for a stellar bubble, the hypersonic stellar wind dominates the region between the star responsible for the bubble and the inner termination shock. Equation (12) of Weaver et al. (1977) states that the distance of the inner shock, R_t is

$$R_t = 0.90 \alpha^{3/2} \left(\frac{1}{\rho_0} \frac{dM_w}{dt} \right)^{3/10} V_w^{1/10} t^{2/5}, \quad (4)$$

where α is a constant equal to 0.88, ρ_0 is the mass density in the external ISM, dM_w/dt is the mass loss rate, V_w is the terminal wind speed, and t is time. For a rough estimate of the inner shock distance, we utilize general stellar parameters for OCl 352 of $dM_w/dt = 10^{-5} M_\odot \text{ yr}^{-1}$, $t = 10^6 \text{ yr}$, and $V_w = 2200 \text{ km s}^{-1}$ (see Section 1.2 or Table 7). From the discussion in Section 6.2, we adopt $n_0 = 4.5 \text{ cm}^{-3}$ for $\rho_0 = n_0 m_p$, where m_p is the mass of a proton. With these values in the appropriate SI units, $R_t \sim 6 \text{ pc}$. It is possible that the line of sight to W4-I18 passes inside the inner shock, and the large, positive RM is due to material modified by the hypersonic stellar wind and not the shocked interstellar material. Because the inner shock is interior to the contact discontinuity between the stellar wind and the ambient ISM, the magnetic field close to the star cluster may be oriented in any direction relative to the exterior (upstream) field. With a positive value of the RM for W4-I18, the line of sight component of the field points toward us while the remaining lines of sight in the cavity are negative, meaning B_{LOS} points away.

5.5. Low Rotation Measure Values Through the W4 Superbubble

North of IC 1805 is the W4 Superbubble, which is an extended “egg-shaped” structure closed at $b \sim 7^\circ$ (West et al. 2007). Basu et al. (1999) utilize an $\text{H}\alpha$ map to define the shape, which would include the southern loop ($134^\circ < \ell < 136^\circ$, $b < 0.5^\circ$); Normandeau et al. (1996) examine the HI distribution, however, and place the base of the structure at OCl 352. Similarly, West et al. (2007) place an offset bottom of the “egg” at OCl 352. The southern loop of IC 1805 is seemingly sufficiently different from the northern latitudes, as it is often not included in the discussion of the W4 Superbubble in spite of the fact that OCl 352 is thought to be responsible for the formation of both structures (Terebey et al. 2003; West et al. 2007).

Nine lines of sight in the present study are north of OCl 352 in the W4 Superbubble. These sources are W4-I1, -I4, -I8, -I12, -I14, -I17, -O4, -O6, and -O7, and they have a mean RM of -293 rad m^{-2} and a standard deviation of 178 rad m^{-2} . Of these sources, W4-I14 and -I17 have the largest RM values, -666 rad m^{-2} and -460 rad m^{-2} , respectively, and they are close to OCl 352, with distances of 31 arcminutes (20 pc) and 17 arcminutes (11 pc), respectively. As discussed in Section 1.2, Lagrois & Joncas (2009a) argue that the ionized “v” structure north of OCl 352 is part of the bubble wall and not a cap to southern loop structure, but examination of Figure 2 suggests that the bubble walls are denser, or thicker, at latitudes $< 1.5^\circ$ than higher latitudes, which may

explain the larger RM associated with W4-I14 and -I17. The remaining lines of sight, however, in the W4 Superbubble have some of the lowest RM values in the data set and are consistently lower RM values than the lines of sight through the PDR.

At higher latitudes, Gao et al. (2015) modeled the polarized emission and applied a Faraday screen model to the W4 Superbubble. They report RMs on the western side of W4 ($\ell \sim 132^\circ$, $b \sim 4.8^\circ$) between -70 and -300 rad m^{-2} and $\sim +55 \text{ rad m}^{-2}$ for the eastern shell ($\ell \sim 136^\circ$, $b \sim 7^\circ$). Gao et al. (2015) argue that since W4 is tilted at an angle towards the observer (Normandeau et al. 1997), a change in the sign of the RM is consistent with a scenario in which the superbubble lifts up a clockwise running Galactic magnetic field (Han et al. 2006) out of the Galactic plane. The magnetic field would go up the eastern side of the superbubble and then down the western side, resulting in the field being pointed toward the observer in the east and away from the observer in the west. While the lines of sight reported in this paper are at $b < 2^\circ$, we find a similar range of RM values as reported by Gao et al. (2015) for the western side. However, we measure RM values 3 – 4.5 times higher on the eastern side, and we do not observe a sign reversal on the eastern side as suggested by Gao et al. (2015).

West et al. (2007) report positive values of the magnetic field for the western side from a change in polarization position angle of $\sim 60^\circ$ at 21 cm, which gives a RM value on order of 20 rad m^{-2} . We do not observe RM values this low for any of our lines of sight through the northern latitudes. Our lines of sight, however, do not probe the same regions as the West et al. (2007) and Gao et al. (2015) studies.

The line of sight W4-I4 is arguably within the W4 Superbubble; however, it is also ~ 8 arcmin (5 pc) on the sky from W3-North (G133.8 +1.4), which is a star forming region within W3. W4-I4 has two components, separated by 15 arcsec (0.2 pc), and a difference in RM values between the two components of $\Delta\text{RM} = 85 \text{ rad m}^{-2}$. The RM values for both components are low (-153 rad m^{-2} and -68 rad m^{-2}) despite being in the superbubble and near to W3, which may have variable but potentially large magnetic fields (van der Werf & Goss 1990; Roberts et al. 1993) (see Section 1.2).

6. Models for the Structure of the H II region and Stellar Bubble

6.1. Whiting et al. (2009) Model of the Rotation Measure in the Shell of a Magnetized Bubble

Whiting et al. (2009) developed a simple analytical shell model intended to represent the Faraday rotation due to a Weaver et al. (1977) solution for a wind-blown bubble. We employed this model in Savage et al. (2013) and Costa et al. (2016) to model the magnitude of the RM in the shell of the Rosette Nebula as a function of distance from the exciting star cluster. Figure 6 of Whiting et al. (2009) and their Section 5.1 give the details of the model, and Sections 4.1

of Savage et al. (2013) and 5 of Costa et al. (2016) describe the application of the model to the Rosette Nebula. This model takes as inputs the general interstellar magnetic field (\mathbf{B}) in μG , the inner (R_1) and outer (R_0) radii of the shell in parsecs, and the electron density in the shell, n_e (cm^{-3}). R_0 represents the shock between the ambient ISM and the shocked, compressed ISM, and R_1 separates the shocked ISM from the hot, diffuse stellar wind in the cavity. Only the component of the ambient interstellar magnetic field that is perpendicular to the shock normal is amplified by the density compression ratio, X . The resulting expression for the RM through the shell is

$$\text{RM} = C n_e L(\xi) B_{0z} \left(1 + (X - 1) \left(\frac{\xi}{R_0} \right)^2 \right), \quad (5)$$

where $L(\xi)$ is the cord length through the shell in parsecs (see Equation 10 in Whiting et al. 2009 or Equation 6 in Costa et al. 2016), and B_{0z} is the z -component of \mathbf{B}_0 , the magnetic field in the ISM. If n_e has units of cm^{-3} , B_{0z} is in μG , and L is in parsecs, $C = 0.81$ (see Equation 2). B_{0z} is at an angle Θ with respect to the LOS and is written as

$$B_{0z} = B_0 \cos \Theta. \quad (6)$$

In our previous work, we presented two cases for the behavior of the magnetic field in the shell. The first is that the magnetic field is amplified by a factor of 4 in the shell. The second case, in which there is not an amplification of the magnetic field in the shell, sets $X = 1$. Equation 5 then simplifies to

$$\text{RM}(\xi) = 0.81 n_e L(\xi) B_{0z}. \quad (7)$$

In Costa et al. (2016), we employed a Bayesian analysis to determine which of the two models better reproduces the observed dependence of the RM as a function of distance. We found that neither model was strongly favored in the case of the Rosette. The model given in Equation (5) is subject to the criticism that it applies shock jump conditions for \mathbf{B} over a large volume of a shell, and that the outer radius of an observed H II region need not be the outer shock of a Weaver bubble (see remarks in Section 5.1.1 of Costa et al. 2016). It is worth including this model, however, in our analysis of IC 1805 for completeness and in order to compare our results to those of the Rosette Nebula.

In Section 1.2, we discussed the the structure of IC 1805, and we present evidence from the literature that north of OCl 352 is part of the W4 Superbubble. Thus, lines of sight north of OCl 352 may have different model parameters for the shell radii and electron density than the southern loop. For the southern latitudes, we utilize the Terebey et al. (2003) thin and thick shell values for the shell radii and electron density. The remaining parameters in Equation (7) are B_0 and Θ . As in Savage et al. (2013) and Costa et al. (2016), we adopt $B_0 = 4 \mu\text{G}$ for the general Galactic field in front of the H II region. The angle Θ is calculated as follows. Assuming a distance of 8.5 kpc to the Galactic center, a distance to OCl 352 of 2.2 kpc, and given a Galactic longitude of 135° ,

the angle between the line of sight and an azimuthal magnetic field is $\Theta = 55^\circ$. We discuss our comparison of this model with the data in Section 7.

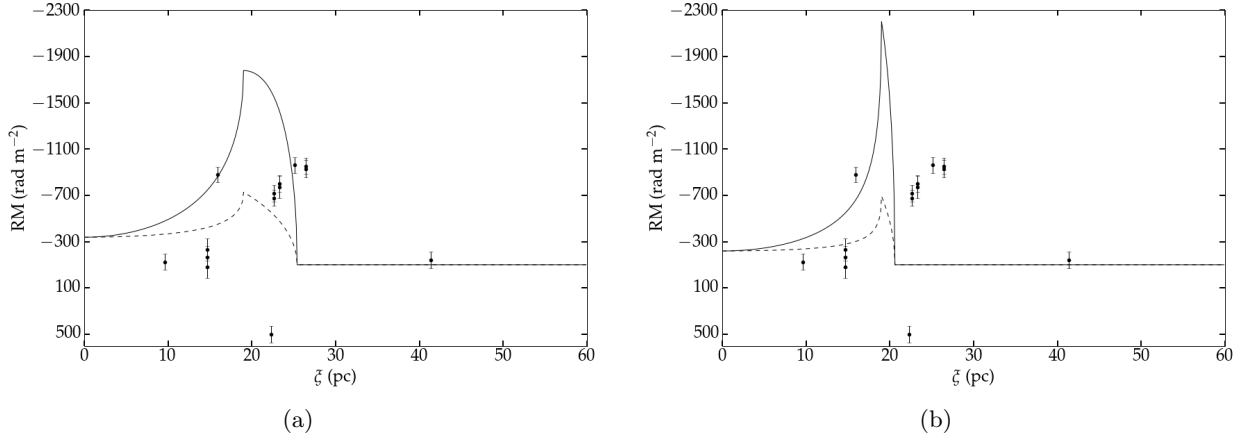


Fig. 10.— Plots of LOS versus distance with the Whiting et al. (2009) model for $X = 4$ (solid) and $X = 1$ (dashed) for $b < +0.9^\circ$ using (a) the thick shell and (b) the thin shell parameters from Terebey et al. (2003). The background $\text{RM} = -100 \text{ rad m}^{-2}$ from the Van Eck et al. (2011) model. The errors on the RM values include the measurement errors and an expected deviation of $\sim 67 \text{ rad m}^{-2}$ from the Van Eck et al. (2011) model. See Table 6 for model parameters.

6.2. Analytical Approximation to Magnetized Bubbles of Ferrière et al. (1991)

Ferrière et al. (1991) presented a semi-analytic discussion of the evolution of a stellar bubble in a magnetized interstellar medium. The theoretical object discussed by Ferrière et al. (1991) could describe a shock wave produced by a supernova explosion or energy input due to a stellar wind. The main features of the model were an outer boundary (e.g. outer shock) which was the first interface between the undisturbed ISM and the bubble, and an inner contact discontinuity between ISM material, albeit modified by the bubble, and matter that originated from the central star or star cluster.

The main feature of the model is that plasma passing through the outer boundary is concentrated in a region between the outer boundary and the contact discontinuity. In what follows, we will refer to this region as the shell of the bubble. The equation of continuity then indicates that there will be higher plasma density in the shell, and the law of magnetic flux conservation indicates that there will be an increase in the strength of the magnetic field in the shell relative to the general ISM field. Ferrière et al. (1991) were interested in the structure of the bubble, and their results have been corroborated by the fully numerical studies of Stil et al. (2009). However, Ferrière et al. (1991) did not calculate the Faraday rotation measure through their model for diagnostic purposes. Stil et al. (2009) explicitly considered the model RMs from their calculations, but only for a couple

to Figure 1 and Figure 4 from Ferrière et al. (1991). An important feature of Figure 11, not present in Ferrière et al. (1991), is the orientation of the line of sight at an angle Θ with respect to the ISM magnetic field at the position of the bubble, and the impact parameter ξ indicating the separation of the LOS from the center of the bubble. The region interior to the contact discontinuity is referred to as the cavity, and for the purposes of our discussion will be considered a vacuum. Another important shell parameter is the thickness $\Delta R \equiv R_s - R_i$, where R_s and R_i are the outer radius of the bubble and the radius of the contact discontinuity, respectively (see Figure 11). We also define and use the dimensionless shell thickness

$$\epsilon \equiv \frac{\Delta R}{R_s} \quad (8)$$

A major simplification that we adopt, based on an approximation of the results of Ferrière et al. (1991), is that the magnetic field in the shell (\mathbf{B}_s) is entirely in the azimuthal direction, and that we ignore radial variations within the shell, i.e.

$$\mathbf{B}_s(r, \theta) \equiv \pm B_s(\theta) \hat{e}_\theta \quad (9)$$

where \hat{e}_θ is a unit vector in the azimuthal direction, and the \pm is selected by the polarity of the interstellar field at the bubble.

We need expressions for the electron density and vector magnetic field within the shell, as well as the geometry of the line of sight. The most important aspect of the Ferrière et al. (1991) theory is the conservation of magnetic flux as the magnetic field in the external medium is swept up and accumulated in the shell. This results in the azimuthal component of the magnetic field increasing as θ increases from 0 to $\frac{\pi}{2}$, as given by Equation (40) of Ferrière et al. (1991). In Ferrière et al. (1991) the shell thickness also depends on θ (Equation 46 of Ferrière et al. 1991), and as a consequence, so does the plasma density in the shell n_s (Equation 38 of that paper).

In the initial version of this paper, we calculated the RM through model bubbles in which B_s , n_s , and ΔR all varied with θ as prescribed by Ferrière et al. (1991). These calculations utilized an approximate form for lines of sight that intersected the bubble in two segments (passing through the central cavity between), and a form that contained a numerically-evaluated expression for lines of sight that remained within the shell from ingress to egress. The algebraic distinction between these 2 cases is discussed below (Sections 6.2.1 and 6.2.2). These expressions for $\text{RM}(\xi)$, including a comparison with our RM measurements, are given in Costa (2018). After examining the results of these calculations, it was decided to simplify our bubble model to that of a spherical shell with constant ϵ . The motivation for this suggestion was the very limited success of the more general model in representing our data, which did not justify the extensive algebraic presentation and non-compact expressions that resulted. The calculations with the approximation of constant ϵ are presented below.

Due to magnetic flux conservation, the expanding shell (now approximated as spherical) will have a magnetic field that is larger than in the external medium, and increases with θ , as in the

original discussion of Ferrière et al. (1991). For our spherical case, it may be shown that the magnetic field in the shell is

$$B_s(\theta) = \frac{B_0}{2\epsilon} \sin \theta \quad (10)$$

where B_0 is the magnitude of the magnetic field in the external medium. The dimensionless shell thickness ϵ remains a free parameter of the model, or one that can be determined by observations. Finally, the plasma density in the shell, determined by mass conservation, is

$$n_s = \frac{n_0}{3\epsilon} \quad (11)$$

where n_0 is the plasma density in the external medium. Equation (11) is a valid approximation for $\epsilon \ll 1$.

6.2.1. RM Calculation for Lines of Sight Through the Walls of the Shell

In evaluating the integral Equation (1) or (2) through the model shell shown in Figure 11, we consider two cases. The first calculation is for lines of sight that pass through a portion of the shell, emerge into the cavity, and then reenter the shell on the opposite side before exiting the shell entirely. This is the case illustrated in Figure 11. The incremental RM for a spatial interval ds along the line of sight is

$$d(\text{RM}) = \pm C n_s B_s(\theta) (\hat{e}_s \cdot \hat{e}_\theta) ds \quad (12)$$

The \pm in front of the RHS indicates that the polarity of the field in the external medium determines the sign of the measured RM. We introduce the variable s as a coordinate along the line of sight; ds is an incremental vector along the line of sight from the source to the observer, and \hat{e}_s is the corresponding unit vector. The constant C is the same as introduced in Equation (5).

It is convenient to change the variable of integration over the LOS from s to ϕ , an angle defined in Figure 11. With the introduction of this variable, the term $(\hat{e}_s \cdot \hat{e}_\theta) = -\sin \phi$. Integration through the shell segments along the line of sight then corresponds to an appropriate integration over ϕ . The shell segment closest to the observer corresponds to an integration from ϕ_1 to ϕ_2 , and the segment furthest from the observer is given by an integration from ϕ_3 to ϕ_4 .

Substitution of Equations (10) and (11) into (12), followed by integration over ϕ and straightforward algebraic manipulation yields the following expression for the RM

$$\text{RM}(x) = \pm \left(\frac{C n_0 B_0 R_s}{3\epsilon^2} \right) x \left[\arcsin \left(\frac{x}{1-\epsilon} \right) - \arcsin(x) \right] \cos \Theta \quad (13)$$

where the new dependent variable is the normalized impact parameter $x \equiv \frac{\xi}{R_s}$. The identity (11) may be used to convert Equation (13) into a form in which the observed plasma density in the shell (n_s) is the density parameter rather than that in the external medium (n_0). This substitution makes Equation (13) more directly comparable to Equation (5).

6.2.2. RM for Lines of Sight Entirely Within the Shell

If the “impact parameter” ξ is sufficiently large, the entire line of sight is within the shell from the point of ingress to that of egress. From Figure 11, it can be seen that this occurs if

$$x \equiv \frac{\xi}{R_s} \geq x_{min} = 1 - \epsilon \quad (14)$$

The RM in this case is a simple generalization of the algebra involved in obtaining Equation (13) via an integration over the angular variable ϕ ; the upper limit of integration in the segment closest to the observer $\phi_2 \rightarrow \frac{\pi}{2}$, and the lower limit of integration for the shell segment further from the observer $\phi_3 \rightarrow \frac{\pi}{2}$.

$$\text{RM}(x) = \pm \left(\frac{C n_0 B_0 R_s}{3\epsilon^2} \right) x \left[\frac{\pi}{2} - \arcsin(x) \right] \cos \Theta, \text{ if: } x_{min} \leq x \leq 1 \quad (15)$$

A plot of the expression $\text{RM}(x)$ given by (13) and (15) is shown in Figure 12 for a set of parameters that are representative for the IC 1805 H II region (see Table 6). The curve is very similar in form to the Whiting model, for the case of no magnetic compression, Equation (5) with $X = 1$ or Equation (7). The model expression for $\text{RM}(x)$ is dependent on n_0 (or the shell density n_s), B_0 , R_s , Θ , and ϵ , the shell thickness parameter. For comparison with observations, we also need to specify the background Galactic rotation measure, RM_{off} .

Our simple model contained in Equations (13) and (15) immediately accounts for one of the main results emergent from the numerical simulations of Stil et al. (2009). The RM through a bubble is maximized when the LOS is parallel to \mathbf{B}_0 ($\cos \Theta = 1$) and small or zero when the LOS is \perp to \mathbf{B}_0 ($\cos \Theta = 0$).

7. Discussion of Observational Results

7.1. Comparison of Models with Observations in the H II Region

In this section we discuss the results of the two models presented in Sections 6.1 and 6.2. In both cases, we adopt the Terebey et al. (2003) center for geometric ease and spherical symmetry as well as the parameters given in their Table 3 for a thick shell.

Figures 10a and 10b show model RM values for lines of sight south of IC 1805 ($b < 0.9^\circ$) with the Whiting et al. (2009) model for the RM as a function of distance and the shell parameters from Terebey et al. (2003). Table 6 gives the values of the center of the bubble, the shell radii, the electron density, X , and Θ for Figure 10. Neither model reliably reproduces the observed RM as a function of distance, and as in Costa et al. (2016), the model can not account for the dispersion of RM values at similar distances. Generally, the lines of sight in the cavity are low and are more consistent with the background RM. In the thin shell approximation, the largest RM values are associated with lines of sight outside the shell. While the model without amplification of the magnetic field in the

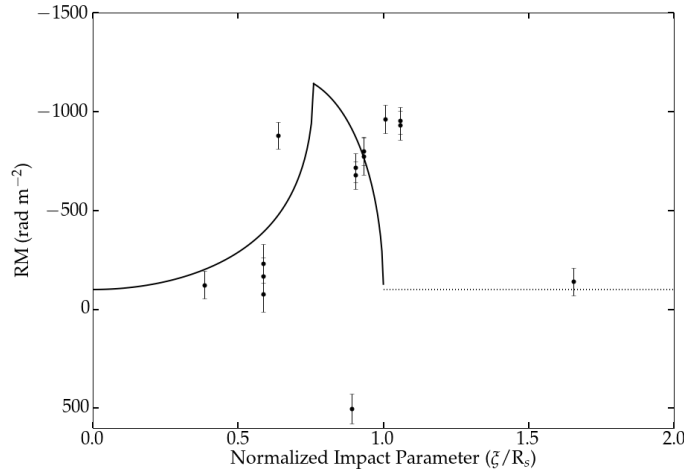


Fig. 12.— Model for the analytic approximation to the bubble model of Ferrière et al. (1991), Equations (13) and (14). The model RM is function of the normalized impact parameter $x = \frac{\xi}{R_s}$. The plotted points represent measured RMs presented in this paper.

shell can marginally account for the magnitude of the RM, the model with amplification (Equation 5) predicts far too high values for the RM for $\Theta = 55^\circ$. The analysis contained here mildly supports a result from Costa et al. (2016) for the Rosette Nebula; Faraday rotation values through these H II regions do not permit a substantial increase in $|B|$ over the general Galactic field.

To reproduce the observed RM in the shell at $\xi \sim 20$ pc, the angle between the magnetic field and the observer would need to be tilted more into the plane of the sky for the $X = 4$ case or into the line of sight for the $X = 1$ case. For the former case, an angle of $\sim 75^\circ$ would reproduce the magnitude of the RM in the shell; such an angle is greater than that expected from a geometric argument, even accounting for a magnetic field pitch angle of $\sim 8^\circ$. Also, no one angle can account for the range of the RM values in the cavity.

With our analytic solution for the RM due to a magnetized bubble as described by Ferrière et al. (1991), we can examine the dependence of RM on Θ as well as ξ . The most obvious choice for the latter parameter is $\Theta = 55^\circ$, based on the geometry as described in Section 6.1. Figure 12 shows our model RM(x) for $\Theta = 55^\circ$, with other parameters given in Table 6. Data for sources south of IC 1805 are superposed on the model. Although the model obviously does not reproduce the measurements in detail, it can describe the overall scale of the “rotation measure anomaly” associated with W4, as well as the approximate magnitude of the largest measured RMs ($|RM| \sim 1000 \text{ rad m}^{-2}$). The peak model RM values shown in Figure 12 do not significantly exceed the measured values, unlike the case for the Whiting model with $X = 4$ (see Figure 10). It should be kept in mind that the shell modeled in Figure 12 is the “thick shell model” of Terebey et al. (2003); the center of that shell is not the star cluster OCl 352, as might be expected.

Stil et al. (2009) carried out numerical MHD simulations of the Ferrière bubbles, which are obviously more accurate than our analytic approximations. Furthermore, they specifically consider and calculate the Faraday rotation through their models. However, Stil et al. (2009) only consider $\Theta = 0^\circ$ and $\Theta = 90^\circ$, so the calculations reported in that paper can not explore the changes in RM structure with Θ . Furthermore, the Faraday rotation calculation of Stil et al. (2009) is done when the outer radius $R_s \sim 200$ pc (see Figure 14 of Stil et al. 2009), which is much larger than the structure we are modeling in Section 6.2 of this paper. In what follows, we compare our observations with the results presented in Section 6 of Stil et al. (2009).

If LOS $\parallel \mathbf{B}_{\text{ext}}$, then the highest values of RM will be through the shell closest to the Galactic plane, but the mean RM across the region will be similar to the mean RM exterior to the bubble (see Figure 14 of Stil et al. 2009). Out of the Galactic plane, the RM is 20 – 30% of the mean RM exterior to the bubble. Effectively, the largest RMs will always be found in the Galactic plane, and different lines of sight through the bubble will have varying RM values.

In comparing the simulations of Stil et al. (2009) to our observational results, we find low RM measures for lines of sight through the cavity, though not always low (e.g., W4-I14 and -I17 vs -I15 and -I21). Lines of sight through the shell have generally large RMs, which is inconsistent with a \mathbf{B}_{ext} perpendicular to the LOS. The case of LOS $\parallel \mathbf{B}_{\text{ext}}$ is inconsistent as well because far from the bubble, the RM is low (e.g., W4-O26 vs -I24) even at similar latitudes, and the lines of sight at $b > 1^\circ$ are consistent with the background RM instead of being reduced by 70 – 80%. Unsurprisingly, our results indicate a case somewhere between these two predictions. As a reminder, we note that the largest values of the RM are for lines of sight exterior to the shell, which is not a prediction from Stil et al. (2009), most likely due to their simulations modeling the ionized bubble and not a PDR structure.

7.2. Magnetic Fields in the PDR

In Section 5.3, we examine evidence for a PDR outside the southern loop of IC 1805. Brogan et al. (1999), Troland et al. (2016), and Pellegrini et al. (2007) report large ($\sim 150 \mu\text{G}$) magnetic fields in PDRs associated with the Orion Veil and M17. In the analysis that follows, we attempt to understand the large RM values for lines of sight through the IC 1805 PDR.

If we consider the PDR and the H II region to be in pressure equilibrium and include magnetic pressure in the PDR, then

$$P_{\text{th}}^{\text{H II}} = P_{\text{th}}^{\text{PDR}} + P_{\text{mag}}^{\text{PDR}}, \quad (16)$$

where $P_{\text{th}}^{\text{H II}}$ and $P_{\text{th}}^{\text{PDR}}$ are the thermal pressures in the H II region and PDR, respectively, and $P_{\text{mag}}^{\text{PDR}} = \frac{B^2}{8\pi}$ is the magnetic pressure in the PDR. In the H II region, $P_{\text{th}}^{\text{H II}} = 2n_e^{\text{H II}} k T_{\text{H II}}$, where $n_e^{\text{H II}}$ and $T_{\text{H II}}$ are the electron density and temperature, k is the Boltzmann constant, and the factor of 2 accounts for the contribution from both ions and electrons. For $P_{\text{th}}^{\text{PDR}} = N_{\text{PDR}} k T_{\text{PDR}}$, N_{PDR} and T_{PDR} are the neutral hydrogen density and the temperature in the PDR.

Near the interface of the PDR and the H II region, the electron density in the PDR is governed by photoionization of carbon (Tielens & Hollenbach 1985), so we estimate n_e^{PDR} by

$$n_e^{\text{PDR}} = N_{\text{PDR}} X_C,$$

where X_C is the cosmic abundance of carbon given in Table 1.4 of Draine (2011) ($X_C \sim 2.95 \times 10^{-4}$). Solving for B in Equation (16) gives

$$B = \sqrt{8\pi k(2 n_e^{\text{H II}} T_{\text{H II}} - N_{\text{PDR}} T_{\text{PDR}})}, \quad (17)$$

and inserting it into Equation (2), we express the RM in the PDR as

$$RM = 0.81 L X_C N_{\text{PDR}} \sqrt{8\pi k (2 n_e^{\text{H II}} T_{\text{H II}} - N_{\text{PDR}} T_{\text{PDR}})}. \quad (18)$$

It should be emphasized that this RM estimate is in the nature of an upper limit to the rotation measure through the PDR. The reason is that it is obtained from a value of B , given by Equation (18), which is based on the magnetic pressure $\frac{B^2}{8\pi}$. The magnetic pressure includes contributions from turbulent fluctuations on all scales, as well as that from a mean or large scale field that produces the net Faraday rotation. In general then, a magnetic field value obtained from an estimate of the magnetic pressure will exceed that obtained from a Faraday rotation measurement.

We differentiate Equation (18) with respect to N_{PDR} to find the value of N_{PDR} that maximizes the RM, which is

$$N_{\text{PDR}} = \frac{4 n_e^{\text{H II}} T_{\text{H II}}}{3 T_{\text{PDR}}}. \quad (19)$$

Inserting values of $T_{\text{H II}} = 8000$ K, $n_e^{\text{H II}} = 10 \text{ cm}^{-3}$ (Terebey et al. 2003), and $T_{\text{PDR}} = 100$ K (Tielens & Hollenbach 1985), gives $N_{\text{PDR}} \sim 1000 \text{ cm}^{-3}$, $B \sim 14 \mu\text{G}$ (Eq 17), and $RM \sim 100 \text{ rad m}^{-2}$. The electron density in the H II region is governing the maximum B expected in the PDR given pressure balance. For the IC 1805 H II region, n_e is low compared to M17 ($n_e \sim 560 \text{ cm}^{-3}$) (Pellegrini et al. 2007), which suggests that a high density (pressure) H II region is needed to explain large magnetic fields in the PDR.

Our analysis suggests that a simple pressure balance analysis predicts low RM values from the PDR that are inconsistent with our observations. It appears that a different mechanism is required to achieve the magnetic fields strengths observed in Brogan et al. (1999).

Terebey et al. (2003) discuss an extended halo of ionized emission around the southern loop, which may indicate that there are more free electrons present outside the obvious ionized shell as seen in Figure 2. This may account for the larger values of the RM we observe. It is clear that knowing the electron density in this region and determining the presence of a PDR through observations, such as carbon radio recombination lines, is necessary to understand how the magnetic field is modified in this complex region.

8. A Comparison of IC 1805 and the Rosette Nebula as “Rotation Measure Anomalies”

Table 7: Stellar Parameters

Star Cluster	Star	Type	\dot{M} ($M_{\odot}\text{yr}^{-1}$)	V_{∞} (km/s)	$L_W = \frac{1}{2}\dot{M}v_{\infty}^2$ ^a (erg s ⁻¹)
NGC 2244	HD 46223	O4V(f) ^b	1.6×10^{-6} ^c	3100 ^d	4.8×10^{36}
	HD 46150	O5.5V ^e	2.0×10^{-6} ^c	3100 ^d	6.0×10^{36}
	HD 46202	O9V(f) ^b	6.3×10^{-8} ^c	1150 ^d	2.6×10^{34}
	HD 46149	O8.5V(f) ^b	2.0×10^{-7} ^c	1700 ^f	1.8×10^{35}
OCI 352	HD15570	O4I ^b	1.0×10^{-5} ^c	2200 ^g	1.5×10^{37}
	HD15558	O4III ^b	6.3×10^{-6} ^c	3000 ^f	1.8×10^{37}
	HD 15629	O5V ^b	2.0×10^{-6} ^c	2900 ^h	5.3×10^{36}

^a Calculated mechanical wind luminosity based on cited mass loss rates and terminal velocities.

^b Massey et al. (1995)

^c Howarth & Prinja (1989)

^d Chlebowski & Garmany (1991)

^e Román-Zúñiga & Lada (2008)

^f Garmany (1988)

^g Bouret et al. (2012)

^h Groenewegen et al. (1989)

We are interested in how the Galactic magnetic field is modified by OB associations via their stellar winds and ionizing photons, and we started our study with the Rosette Nebula, where we found large ($\sim 10^3$ rad m⁻²) RM measurements through the ionized shell of the H II region (Costa et al. 2016).

In the case of the Rosette, we find positive RM across the region, and for IC 1805, we find negative values. If the Galactic magnetic field follows the spiral arms in a clockwise direction, then we would expect the LOS magnetic field component to be pointed towards us (positive B) for $\ell > 180^\circ$, and pointed away from us (negative B) for $\ell < 180^\circ$. Except for one line of sight in each nebula, we find that the polarity of the Galactic magnetic field is preserved across each nebula and is consistent with the large scale field through the arm.

In our study of the Rosette, we investigated whether the magnetic field is amplified in the shell of the nebula. We found that the model without amplification was weakly favored over the case when the magnetic field is amplified in the shell. When we applied the same model to IC 1805, however, it is difficult to conclude in favor of either model, but in both cases, the model with an enhanced magnetic field overpredicts the RM. From inspection of Figures 10a and 10b, it seems that the model without amplification better accounts for the magnitude of the observed RMs, but

the observations do not conform to the model prediction of $\text{RM}(\xi)$, and the model can not account for the wide range in observed values of RM at a given ξ .

In the present study, we find the highest RMs for lines of sight outside the obvious shell structure, though one line of sight (W4-I13) does appear to intersect the ionized shell and it has a large RM. These lines of sight may be probing the magnetic field within the PDR. In the case of the Rosette, we found that the highest RM values were for lines of sight through the bright ionized shell. However with our work on IC 1805 and the PDR associated with it, we have briefly revisited our results in the Rosette, particularly Figure 1 from Costa et al. (2016). There are a few lines of sight with RM of order a few 10^2 rad m^{-2} that appear to be outside the ionized shell. These lines of sight were included in the background estimate for the Rosette, but if the Rosette also has a PDR, then these lines of sight may actually be probing that material.

Table 7 lists spectral type, mass loss rate, terminal wind velocity, and calculated wind luminosity from the literature for O stars with the largest wind luminosities in both NGC 2244, which is associated with the Rosette Nebula, and OCl 352. The sum of the wind luminosities of the three main stars in OCl 352 is 3.8×10^{37} ergs s^{-1} , while the corresponding number for NGC 2244 (4 stars) is 1.1×10^{37} ergs s^{-1} . In addition, OCl 352 appears to have more luminous stars. As such, OCl 352 might be expected to produce a more energetic stellar bubble than NGC 2244. Our Faraday rotation measurements show no indication of this, in that the largest RMs observed are similar for the two objects. In fact, higher RMs were measured for the Rosette than for any line of sight through IC 1805. A number of factors can control the impact a star cluster has on the ISM. If some relationship exists between the total wind luminosity of a star cluster and properties of an interstellar bubble that can be measure with Faraday rotation, it will apparently require a large sample of clusters/ H II regions to reveal it.

9. Future Research

In the future, we will continue our investigation of H II regions and how they modify their surroundings and the Galactic magnetic field. An immediate investigation will be centered on observations of the H II region IC 1396. This will provide a third H II region with different age, stellar content, and Galactic location. The observations are similar to those we have made of the Rosette Nebula and IC 1805. The observations of IC 1396 have been made with the VLA and are awaiting analysis. By adding more H II regions to our study, we can begin to address questions such as

1. Since the electron density distributions in H II regions are known from radio continuum observations, we can inquire what conditions would result in an $\text{RM} \gg 10^3$ rad m^{-2} through the shell of an H II region.
2. Is it a general property of H II regions and stellar bubbles that the polarity of the Galactic

magnetic field is preserved within the region? The answer to this question has implications for the amplitude of MHD turbulence in the ISM on scales of the order of the H II regions, $\sim 10 - 30$ pc.

3. Do PDRs around other nebulae produce high RMs? What is the magnitude of the RM due to the PDR relative to that of the shell of an H II region?

In addition to increasing the number of H II regions, understanding Faraday complexity and how to interpret the associated RM measurements is important to studies of Galactic magnetic fields, particularly with large polarization surveys like the VLA Sky Survey (VLASS) and Polarisation Sky Survey of the Universe’s Magnetism (POSSUM) with the Australian Square Kilometre Array Pathfinder (ASKAP) in the near future.

10. Summary and Conclusions

1. We performed polarimetric observations using the VLA for 27 lines of sight through or near the shell of the H II region and stellar bubble associated with the OB association OCl 352.
2. We obtain RM measurements for 20 sources using two methods. The first is through the traditional least-squares fit to $\chi(\lambda^2)$, and the second is using RM Synthesis. Including components that are resolved, we report 27 RM values, and we find good agreement between the two methods. We find the same sign of the RM across the entire region with the exception of one source, W4-I18. We estimate a background RM due to the general ISM of -145 rad m^{-2} in this part of the Galactic plane. We measure an excess of RM of $\sim +600$ to -800 rad m^{-2} due to W4.
3. Only one line of sight has a positive RM value, W4-I18. It has a RM of $+501 \pm 33$ rad m^{-2} , and it is located 5.6 arcminutes from the center of OCl 352. This line of sight may be probing the material close to the massive stars. The orientation of the line of sight component of the magnetic field is directed towards the observer, whereas in the rest of the region, the magnetic field is directed away.
4. We find that some of the lines of sight with the largest RM values occur just outside the obvious ionized shell of IC 1805 and are potentially probing the magnetic field in the PDR. The lines of sight through the cavity of the bubble have lower RM values than those through the shell. In the W4 Superbubble, which is north of OCl 352, we find RM values consistent with the background RM.
5. We discuss two shell models to reproduce the magnitude of the RM and its dependency on distance from the center of the star cluster. We employed the first of these models in Savage et al. (2013) and Costa et al. (2016), and it is based on the Weaver et al. (1977) solution for a stellar bubble, which includes a shock expanding into an ambient medium. The second model

uses magnetic flux conservation to describe how the magnetic field is modified in the shell and consists of a simplified analytic approximation to the results presented by Ferrière et al. (1991). Neither of these simplified models satisfactorily accounts for the dependence of RM on spatial location within the shell, although the Whiting model without field amplification ($X = 1$) and the simplified Ferrière model approximately reproduce the magnitude of the largest RMs. However, both models predict a single-valued dependence of RM on ξ , the separation of the line of sight from the center of the nebula, whereas the observations show a large range of RM for sources with similar values of ξ .

6. Because we have independent information on the electron density from radio continuum observations of both IC 1805 and the Rosette Nebula, our observations can limit the magnitude of the magnetic field in the H II regions. Our RM measurements indicate that the field does not greatly exceed the value in the general ISM.
7. We compare our results from the current study of IC 1805 and our previous study of the Rosette Nebula. Notably, we find the same order of magnitude for the RM for the two nebulae, but the sign of the RM in each region is opposite. Since IC 1805 and the Rosette are at different Galactic longitudes and on either side of $b = 180^\circ$, the sign difference between the two nebula is consistent with a Galactic magnetic field that follows the spiral arm structure in a clock-wise direction, as suggested in models (Van Eck et al. 2011).

This research was partially supported at the University of Iowa by grants AST09-07911 and ATM09-56901 from the National Science Foundation. This publication makes use of data products from the Wide-field Infrared Survey Explorer (Wright et al. 2010), which is a joint project of the University of California, Los Angeles, and the Jet Propulsion Laboratory/California Institute of Technology, funded by the National Aeronautics and Space Administration. Additionally, the research presented in this paper uses data from the Canadian Galactic Plane Survey, a Canadian project with international partners, supported by the Natural Sciences and Engineering Research Council. This research also uses the Python packages Astropy, a community-developed core Python package for Astronomy (Astropy Collaboration et al. 2013) and NumPy (Van Der Walt et al. 2011). Finally, we thank the referee of this paper for a helpful and collegial review.

REFERENCES

- Albert, J., Aliu, E., Anderhub, H., et al. 2008, *ApJ*, 684, 1351
- Anantharamaiah, K. R. 1985, *Journal of Astrophysics and Astronomy*, 6, 203
- Anderson, C. S., Gaensler, B. M., Feain, I. J., & Franzen, T. M. O. 2015, *ApJ*, 815, 49
- Anderson, L. D., Bania, T. M., Balsler, D. S., et al. 2014, *ApJS*, 212, 1
- Anderson, L. D., Zavagno, A., Barlow, M. J., García-Lario, P., & Noriega-Crespo, A. 2012, *A&A*, 537, A1
- Aragona, C., McSwain, M. V., Grundstrom, E. D., et al. 2009, *ApJ*, 698, 514
- Astropy Collaboration, Robitaille, T. P., Tollerud, E. J., et al. 2013, *A&A*, 558, A33
- Balsler, D. S., Anish Roshi, D., Jeyakumar, S., et al. 2016, *ApJ*, 816, 22
- Basu, S., Johnstone, D., & Martin, P. G. 1999, *ApJ*, 516, 843
- Bell, M. R., & Enßlin, T. A. 2012, *A&A*, 540, A80
- Bignami, G. F., Caraveo, P. A., Lamb, R. C., Markert, T. H., & Paul, J. A. 1981, *ApJ*, 247, L85
- Bignell, C. 1982, in *Synthesis Mapping*, ed. A. R. Thompson & L. R. D’Addario, 6
- Bik, A., Henning, T., Stolte, A., et al. 2012, *ApJ*, 744, 87
- Bouret, J.-C., Hillier, D. J., Lanz, T., & Fullerton, A. W. 2012, *A&A*, 544, A67
- Braunsfurth, E. 1983, *A&A*, 117, 297
- Brentjens, M. A., & de Bruyn, A. G. 2005, *A&A*, 441, 1217
- Brogan, C. L., Troland, T. H., Roberts, D. A., & Crutcher, R. M. 1999, *ApJ*, 515, 304
- Brown, J. C., Taylor, A. R., & Jackel, B. J. 2003, *ApJS*, 145, 213
- Carpenter, J. M., Heyer, M. H., & Snell, R. L. 2000, *ApJS*, 130, 381
- Casares, J., Ribas, I., Paredes, J. M., Martí, J., & Allende Prieto, C. 2005, *MNRAS*, 360, 1105
- Chlebowski, T., & Garmany, C. D. 1991, *ApJ*, 368, 241
- Churchwell, E., Povich, M. S., Allen, D., et al. 2006, *ApJ*, 649, 759
- Cioffi, D. F., & Jones, T. W. 1980, *AJ*, 85, 368
- Condon, J. J., Cotton, W. D., Greisen, E. W., et al. 1998, *AJ*, 115, 1693

- Costa, A. H. 2018, PhD thesis, The University of Iowa
- Costa, A. H., Spangler, S. R., Sink, J. R., Brown, S., & Mao, S. A. 2016, *ApJ*, 821, 92
- Dambis, A. K., Mel'Nik, A. M., & Rastorguev, A. S. 2001, *Astronomy Letters*, 27, 58
- de Avillez, M. A., & Breitschwerdt, D. 2005, *A&A*, 436, 585
- Dennison, B., Topasna, G. A., & Simonetti, J. H. 1997, *ApJ*, 474, L31
- Dhawan, V., Mioduszewski, A., & Rupen, M. 2006, in *VI Microquasar Workshop: Microquasars and Beyond*, 52.1
- Dickel, H. R. 1980, *ApJ*, 238, 829
- Dickel, H. R., Dickel, J. R., Wilson, W. J., & Werner, M. W. 1980, *ApJ*, 237, 711
- Digel, S. W., Lyder, D. A., Philbrick, A. J., Puche, D., & Thaddeus, P. 1996, *ApJ*, 458, 561
- Draine, B. T. 2011, *Physics of the Interstellar and Intergalactic Medium*
- Dubus, G. 2006, *A&A*, 456, 801
- Everett, J. E., & Weisberg, J. M. 2001, *ApJ*, 553, 341
- Farnsworth, D., Rudnick, L., & Brown, S. 2011, *AJ*, 141, 191
- Feigelson, E. D., & Townsley, L. K. 2008, *ApJ*, 673, 354
- Feigelson, E. D., Townsley, L. K., Broos, P. S., et al. 2013, *ApJS*, 209, 26
- Ferrière, K. M., Mac Low, M.-M., & Zweibel, E. G. 1991, *ApJ*, 375, 239
- Frail, D. A., & Hjellming, R. M. 1991, *AJ*, 101, 2126
- Gao, X. Y., Reich, W., Reich, P., Han, J. L., & Kothes, R. 2015, *A&A*, 578, A24
- Garmany, C. D. 1988, *NASA Special Publication*, 497, 160
- Gooch, R. 1995, in *Astronomical Society of the Pacific Conference Series*, Vol. 77, *Astronomical Data Analysis Software and Systems IV*, ed. R. A. Shaw, H. E. Payne, & J. J. E. Hayes, 144
- Gray, A. D., Landecker, T. L., Dewdney, P. E., et al. 1999, *ApJ*, 514, 221
- Gregory, P. C., & Neish, C. 2002, *ApJ*, 580, 1133
- Gregory, P. C., Taylor, A. R., Crampton, D., et al. 1979, *AJ*, 84, 1030
- Groenewegen, M. A. T., Lamers, H. J. G. L. M., & Pauldrach, A. W. A. 1989, *A&A*, 221, 78

- Guetter, H. H., & Vrba, F. J. 1989, *AJ*, 98, 611
- Han, J. L., Manchester, R. N., Lyne, A. G., Qiao, G. J., & van Straten, W. 2006, *ApJ*, 642, 868
- Harvey-Smith, L., Madsen, G. J., & Gaensler, B. M. 2011, *ApJ*, 736, 83
- Hasegawa, T., Sato, F., & Fukui, Y. 1983, *AJ*, 88, 658
- Haverkorn, M., Gaensler, B. M., McClure-Griffiths, N. M., Dickey, J. M., & Green, A. J. 2004, *ApJ*, 609, 776
- Heald, G. 2009, in *IAU Symposium*, Vol. 259, *IAU Symposium*, ed. K. G. Strassmeier, A. G. Kosovichev, & J. E. Beckman, 591–602
- Heyer, M. H., & Terebey, S. 1998, *ApJ*, 502, 265
- Heyer, M. H., Brunt, C., Snell, R. L., et al. 1996, *ApJ*, 464, L175
- Hill, A. S., Landecker, T. L., Carretti, E., et al. 2017, *MNRAS*, 467, 4631
- Hollenbach, D. J., & Tielens, A. G. G. M. 1999, *Reviews of Modern Physics*, 71, 173
- Howarth, I. D., & Prinja, R. K. 1989, *ApJS*, 69, 527
- Jose, J., Kim, J. S., Herczeg, G. J., et al. 2016, *ApJ*, 822, 49
- Kerton, C. R., Arvidsson, K., & Alexander, M. J. 2013, *AJ*, 145, 78
- Kharchenko, N. V., Piskunov, A. E., Röser, S., Schilbach, E., & Scholz, R.-D. 2005, *A&A*, 438, 1163
- Kiminki, M. M., Kim, J. S., Bagley, M. B., Sherry, W. H., & Rieke, G. H. 2015, *ApJ*, 813, 42
- Lagrois, D., & Joncas, G. 2009a, *ApJ*, 691, 1109
- . 2009b, *ApJ*, 693, 186
- Lagrois, D., Joncas, G., & Drissen, L. 2012, *MNRAS*, 420, 2280
- Landecker, T. L., Reich, W., Reid, R. I., et al. 2010, *A&A*, 520, A80
- Lestrade, J.-F., Preston, R. A., Jones, D. L., et al. 1999, *A&A*, 344, 1014
- Macquart, J.-P., Ekers, R. D., Feain, I., & Johnston-Hollitt, M. 2012, *ApJ*, 750, 139
- Mao, S. A., Gaensler, B. M., Haverkorn, M., et al. 2010, *ApJ*, 714, 1170
- Massey, P., Johnson, K. E., & Degioia-Eastwood, K. 1995, *ApJ*, 454, 151
- Massi, M. 2004, *A&A*, 422, 267

- Massi, M., Migliari, S., & Chernyakova, M. 2017, *MNRAS*, 468, 3689
- Massi, M., Ribó, M., Paredes, J. M., et al. 2004, *A&A*, 414, L1
- Moore, T. J. T., Bretherton, D. E., Fujiyoshi, T., et al. 2007, *MNRAS*, 379, 663
- Nakano, M., Soejima, T., Chibueze, J. O., et al. 2017, *PASJ*, 69, 16
- Navarete, F., Figueredo, E., Daminieli, A., et al. 2011, *AJ*, 142, 67
- Normandeau, M., Taylor, A. R., & Dewdney, P. E. 1996, *Nature*, 380, 687
- . 1997, *ApJS*, 108, 279
- Oey, M. S., Watson, A. M., Kern, K., & Walth, G. L. 2005, *AJ*, 129, 393
- O’Sullivan, S. P., Brown, S., Robishaw, T., et al. 2012, *MNRAS*, 421, 3300
- Paredes, J. M., Ribó, M., Bosch-Ramon, V., et al. 2007, *ApJ*, 664, L39
- Pellegrini, E. W., Baldwin, J. A., Brogan, C. L., et al. 2007, *ApJ*, 658, 1119
- Purcell, C. R., Gaensler, B. M., Sun, X. H., et al. 2015, *ApJ*, 804, 22
- Reynolds, R. J., Sterling, N. C., & Haffner, L. M. 2001, *ApJ*, 558, L101
- Roberts, D. A., Crutcher, R. M., Troland, T. H., & Goss, W. M. 1993, *ApJ*, 412, 675
- Román-Zúñiga, C. G., & Lada, E. A. 2008, *Star Formation in the Rosette Complex*, ed. B. Reipurth, 928
- Román-Zúñiga, C. G., Ybarra, J. E., Megías, G. D., et al. 2015, *AJ*, 150, 80
- Roshi, D. A. 2007, *ApJ*, 658, L41
- Sato, F. 1990, *AJ*, 99, 1897
- Savage, A. H., Spangler, S. R., & Fischer, P. D. 2013, *ApJ*, 765, 42
- Shi, H. M., & Hu, J. Y. 1999, *A&AS*, 136, 313
- Sokoloff, D. D., Bykov, A. A., Shukurov, A., et al. 1998, *MNRAS*, 299, 189
- Stil, J., Wityk, N., Ouyed, R., & Taylor, A. R. 2009, *ApJ*, 701, 330
- Sun, X. H., Han, J. L., Reich, W., et al. 2007, *A&A*, 463, 993
- Sun, X. H., Reich, W., Waelkens, A., & Enßlin, T. A. 2008, *A&A*, 477, 573
- Sun, X. H., Landecker, T. L., Gaensler, B. M., et al. 2015, *ApJ*, 811, 40

- Taylor, A. R., Irwin, J. A., Matthews, H. E., & Heyer, M. H. 1999, *ApJ*, 513, 339
- Taylor, A. R., Stil, J. M., & Sunstrum, C. 2009, *ApJ*, 702, 1230
- Taylor, A. R., Gibson, S. J., Peracaula, M., et al. 2003, *AJ*, 125, 3145
- Terebey, S., Fich, M., Taylor, R., Cao, Y., & Hancock, T. 2003, *ApJ*, 590, 906
- Tielens, A. G. G. M., & Hollenbach, D. 1985, *ApJ*, 291, 722
- Tomisaka, K. 1990, *ApJ*, 361, L5
- . 1998, *MNRAS*, 298, 797
- Townsley, L. K., Broos, P. S., Garmire, G. P., et al. 2014, *ApJS*, 213, 1
- Troland, T. H., Goss, W. M., Brogan, C. L., Crutcher, R. M., & Roberts, D. A. 2016, *ApJ*, 825, 2
- Vallée, J. P. 1993, *ApJ*, 419, 670
- Van Der Walt, S., Colbert, S. C., & Varoquaux, G. 2011, *Computing in Science & Engineering*, 13, 22
- van der Werf, P. P., & Goss, W. M. 1990, *A&A*, 238, 296
- Van Eck, C. L., Brown, J. C., Stil, J. M., et al. 2011, *ApJ*, 728, 97
- Watson, C., Povich, M. S., Churchwell, E. B., et al. 2008, *ApJ*, 681, 1341
- Weaver, R., McCray, R., Castor, J., Shapiro, P., & Moore, R. 1977, *ApJ*, 218, 377
- West, J. L., English, J., Normandeau, M., & Landecker, T. L. 2007, *ApJ*, 656, 914
- Whiting, C. A., Spangler, S. R., Ingleby, L. D., & Haffner, L. M. 2009, *ApJ*, 694, 1452
- Wright, E. L., Eisenhardt, P. R. M., Mainzer, A. K., et al. 2010, *AJ*, 140, 1868